ADDITIVE MANUFACTURING OF PASSIVE BEAMFORMING SYSTEMS

by

Austin J Good

A dissertation submitted to the Faculty of the University of Delaware in partial fulfillment of the requirements for the degree of Doctor of Philosophy in Electrical and Computer Engineering

Spring 2019

ADDITIVE MANUFACTURING OF PASSIVE BEAMFORMING SYSTEMS

by

Austin Good

Approved: _____
Kenneth E. Barner, Ph.D.
Chair of the Department of Electrical and Computer Engineering

Approved: _____
Levi Thompson, Ph.D.
Dean of the College of Engineering

Approved: _____
Douglas J. Doren, Ph.D.
Interim Vice Provost for Graduate and Professional Education

I certify that I have read this dissertation and that in my opinion it meets the academic and professional standard required by the University as a dissertation for the degree of Doctor of Philosophy.

Signed: _____

Mark Mirotznik, Ph.D.
Professor in charge of dissertation

I certify that I have read this dissertation and that in my opinion it meets the academic and professional standard required by the University as a dissertation for the degree of Doctor of Philosophy.

Signed: _____

Richard Martin, Ph.D.
Member of dissertation committee

I certify that I have read this dissertation and that in my opinion it meets the academic and professional standard required by the University as a dissertation for the degree of Doctor of Philosophy.

Signed: _____

John Suarez, Ph.D.
Member of dissertation committee

I certify that I have read this dissertation and that in my opinion it meets the academic and professional standard required by the University as a dissertation for the degree of Doctor of Philosophy.

Signed: _____

Paul Ransom, Ph.D.
Member of dissertation committee

I certify that I have read this dissertation and that in my opinion it meets the academic and professional standard required by the University as a dissertation for the degree of Doctor of Philosophy.

Signed: _____

Shridhar Yarlagadda, Ph.D.
Member of dissertation committee

ACKNOWLEDGMENTS

I would like to thank my advisor, Dr. “Big Dog” Mirotznik, for his help and guidance on this work. I would also like to thank my peers: Matthew Mills, Peter Pa, Zachary Larimore, Paul Parsons, Nicholas Hudak, and Siddartha Garrett. Their assistance and advice made the research for my thesis a wonderful experience. I also would like to thank everyone in Dr. Mirotznik’s group for maintaining a fun and upbeat work environment; it made research a fun yet productive experience.

I would like to dedicate this work to my parents: Michael and Danette Good. I could not have asked for better parents. They have always been there for me during the stressful moments in my life. I am blessed to have their love and support.

TABLE OF CONTENTS

LIST OF TABLES

LIST OF FIGURES

ABSTRACT

The ability to control electromagnetic wave propagation using spatially varying or graded index of refraction (GRIN) structures have resulted in a number of practical photonic devices (e.g., GRIN lenses and graded index optical fibers). At radiofrequencies (RF), GRIN structures have also been explored for their use as lens antennas, antireflective surfaces, and passive beam formers. For the specific application of RF beamforming, GRIN structures provide a particularly cost effective solution, however, their design and fabrication can often be a major challenge. In this dissertation, I will describe two novel methods that leveraged recent advances in additive manufacturing (AM), and how I applied them towards the fabrication of RF beamforming systems. Specifically, these methods are; (1) multimaterial AM of 3D graded index lenses and (2) custom system for dry powder printing of ceramics for structural beamforming applications.

Chapter 1

INTRODUCTION

1.1 Motivation

Beamforming is a process in which radiation can be emitted or received in a particular direction or directions, thus providing spatial selectivity. Passive and active beamforming systems achieve this goal through different approaches. Active beamforming systems interferometrically combine an array of sensors to propagate or receive power in a desired direction. To do so requires, the use of active RF circuitry that combines low noise amplifiers, phase shifters, and mixers. In contrast, passive beamforming uses a passive lens based system to achieve beam steering. There are a number of pros and cons to each of these approaches with size, weight, cost, and bandwidth requirements as important considerations.

Passive beamforming has a few distinct advantages over traditional active beamforming systems. First, passive beamforming systems are true time delay (TTD) devices. TTD means that there is a linear relationship between phase and frequency as long as the materials are nondispersive. As a result of TTD, passive beamforming systems are inherently broadband. A second advantage is that fabricating a three-dimensional passive beamforming system is less complicated than a three-dimensional active beamforming system. Lastly, passive beamforming systems are significantly less expensive. Given the simplicity and lower cost of passive beamforming systems, I will explore the design and fabrication of passive beamforming systems through additive manufacturing.

1.2 Literature Review on Beamforming

Beamforming technology has been steadily evolving since Heinrich Hertz invented the parabolic antenna in 1887 [1]. Parabolic antennas are usually large and heavy and to redirect the antenna, you must mechanically reposition the direction it is facing. Thus, requiring powerful motors in addition to the parabolic antenna. The need for electronic beam steering with no moving parts fueled the next 100 years of beamforming research. In the 1940s, technology became available to control the phase shift at an antenna element [2]. By changing the phase shift delay of each antenna in an antenna array, it is possible to scan a high gain beam in various directions. This technology has given birth to electrically steerable arrays used for SATCOM, ballistic missile detection/tracking, and other long range warning systems. Some notable systems include: Cobra Dane, PAVE PAWS, and SPY-1.

Figure 1.1: Images of the (left to right) Cobra Dane [3], PAVE PAWS [4], and SPY-1 [5] radar systems

Unfortunately, the electrically steered arrays listed above come at a multimillion dollar cost [5-7]. Parabolic antennas are a fraction of the cost, but as

mentioned earlier, are very heavy and need to be mechanically steered. As an alternative, there passive high gain structures for gain enhancement, much like the parabolic antenna. These structures include the Luneburg lens [8], Maxwell Fisheye [9], Fresnel lens [10], and the Rotman lens [12]. These systems differ in that there are a discrete number of excitation positions. Because of discrete excitation positions, these systems are more commonly referred to as beam switching systems (Figure 1.2).

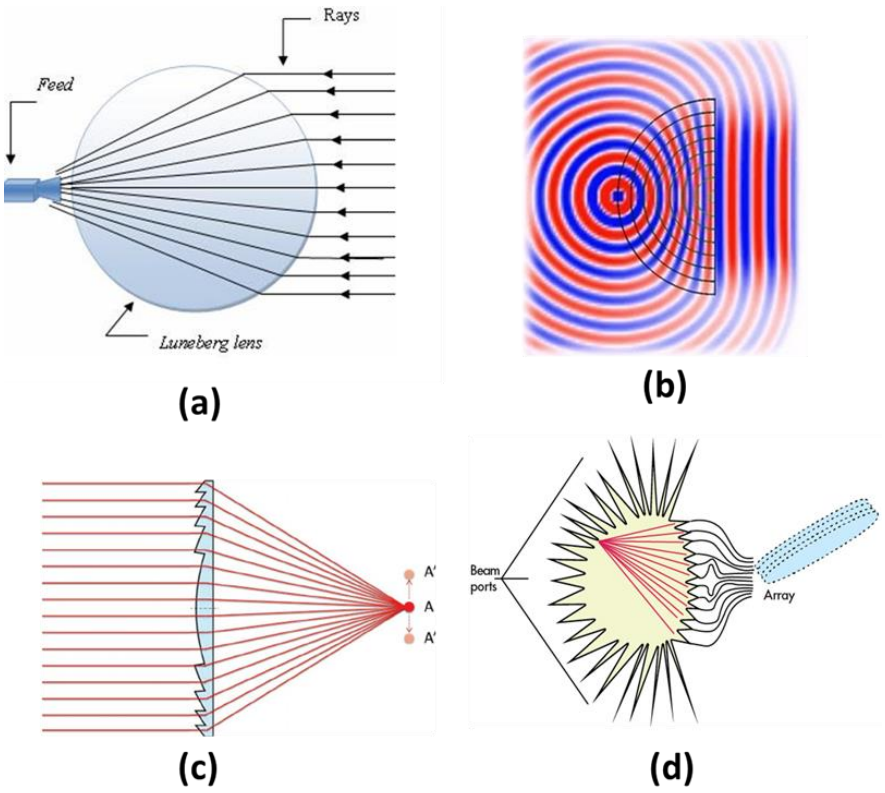

Figure 1.2: Illustration of gain enhancement systems. a) Luneburg lens [12], b) Half Maxwell Fisheye [13], c) Fresnel zone lens [14], d) Rotman lens [15]

The work in this dissertation primarily covers graded refractive index (GRIN) lenses for passive beamforming. Therefore, I will explain common manufacturing methods for GRIN structures such as the Luneburg lens and the Maxwell Fisheye lens.

One popular technique is subtractive manufacturing. This method utilizes computer numerical control (CNC) milling to create spatially varying air voids within a solid homogenous dielectric [16-17]. Assuming the void size and spacing are much smaller than the wavelength, the combination of air pockets and background create a locally varying effective permittivity. Unfortunately, for many applications, drilling air pockets into a substrate significantly compromises the structural integrity of the device.

A second popular technique leverages constructing concentric layers of discretely varying dielectric constant values [17-20]. This can be achieved by having a library of machinable materials to form concentric shells to makeup a sphere or a cylinder. Another similar method uses a dielectric foam/porous material that is compressed to increase the material's density and effective dielectric constant [18]. Two significant disadvantages to these techniques: it requires a large library of materials to achieve the desired dielectric layers, and these processed require a vast amount of human intervention throughout the fabrication process. The additive manufacturing process I use in this dissertation requires no human intervention.

1.3 List of Publications

The following publications are first author publications:

1. **A. Good**, D. Roper, B. Good, S. Yarlagadda, and M. Mirotznik. "Multifunctional Graded Dielectrics Fabricated Using Dry Powder Printing." Smart Materials and Structures. Vol 26. Issue 9. 14 August 2017

2. J. Deroba*, **A. Good***, K. Sobczak, Z. Larimore, and M. Mirotznik. "Additively Manufactured Luneburg Retroreflector." IEEE Aerospace & Electronics Systems Magazine. Submitted on 1 January 2019. (* - equal contributions)

3. **A. Good**, J. Suarez, R. Martin, Z Larimore, N Hudak, and M. Mirotznik. "Low cost platform for passive imaging of RF emitters using Luneburg lenses" Electronic Letters. Submitted on 12 March 2019.

The following publications are additional contributions while pursuing my Ph.D.:

4. B. Good, P. Ransom, S. Simmons, **A. Good**, and M. Mirotznik. "Design of Graded Index Flat Lenses with Integrated Antireflective Properties." Microwave and Optical Technology Letters. Vol 54. Issue 12. December 2012.

5. D. Roper, B. Good, R. McCauley, S. Yarlagadda, J. Smith, **A. Good**, P. Pa, and M. Mirotznik. "Additive Manufacturing of Graded Dielectrics." Smart Materials and Structures. Vol 23. Issue 4. 3 June 2014

6. B. Good, D. Roper, **A. Good**, and M. Mirotznik. "Effective Media Theory of Dry Powder Dot Printing." 2016 IEEE International Symposium on Antennas and Propagation (APS/URSI). 26 June 2016.

7. Z. Larimore, S. Jensen, **A. Good**, A. Lu, J. Suarez, and M. Mirotznik. "Additive Manufacturing of Luneburg Lens Antennas Using Space-Filling Curves and Fused Filament Fabrication." IEEE Transactions on Antennas and Propagation. Vol 66. Issue 6. June 2018.

8. M. Mirotznik, Z. Larimore, P. Parsons, and **A. Good**. "Additively Manufactured RF Devices and Systems." 2018 IEEE International Symposium on Antennas and Propagation & USNC/URSI National Radio Science Meeting. 13 July 2018.

9. S. Biswas, A. Lu, Z Larimore, P. Parsons, **A. Good**, J Suarez, and M. Mirotznik. "Realization of Modified Luneburg Lens Antenna Using Quasi-Conformal Transformation Optics and Additive Manufacturing." Microwave and Optical Technology Letters. 29 December 2018.

10. Z. Larimore, **A. Good**, J. Suarez, P. Parsons and M.S. Mirotznik, "Additive Manufacturing of snap-on RF connectors", submitted to Additive Manufacturing, March 2019.

1.4 List of Contributions

There were a number of original contributions that came from my research:

- Development of a novel dry powder deposition system and characterized the electromagnetic properties of the combined materials.
- Using my custom dry powder printer, I fabricated a structurally robust 2D passive beamforming lens.
- I conducted a comprehensive tradeoff study on 3D Luneburg lenses including the relationship between size, weight, gain, bandwidth, and cost projections of additively manufactured 3D Luneburg lenses
- I designed, fabricated, and tested a 3D Luneburg lens based retroreflector
- I designed, fabricated, and tested a 3D Luneburg lens based detection and tracking system for multiple RF emitters.

1.5 Dissertation Outline

In Chapter 2, I provide an overview of the various additive manufacturing methods and additive manufacturing materials. Then, I will establish the most suitable materials and additive manufacturing methods for RF applications such as passive beamforming. In Chapter 3, I discuss the various methods of beamforming and discuss the pros and cons of each method. In Chapter 4, I will present a custom dry powder printing system that was used to additively manufacture a 2D passive beamforming system. In Chapter 5, I discuss the use fused deposition modelling (FDM) to create 3D Luneburg lenses for use as 3D beamforming. Using these Luneburg lenses, I was able

to fabricate two unique beamforming systems: (1) ultra-wideband RF retroreflector and (2) ultra-wideband RF directional finder. Lastly in Chapter 6, I will share my closing thoughts and future directions of this work.

Chapter 2

BACKGROUND ON ADDITIVE MANUFACTURING SYSTEMS AND MATERIALS

2.1 Overview of Additive Manufacturing Methods

In this section, I will describe various additive manufacturing techniques as well as their advantages and disadvantages when applied towards the application of passive beamforming.

2.1.1 Vat Polymerization

As in all current 3D printing processes, vat polymerization is a layer-by-layer 3D printing technique. In vat polymerization, a large pool of ultraviolet (UV) curable resin is combined with a UV light source to selectively cure resin where desired. The 3D printing process is as follows. The build plate starts near the surface of the UV curable resin vat where the light is rastered to cure the first layer. The build plate then drops one layer deeper into the vat, and the UV light rasters again to complete the next layer. This process is continued as many times as needed to complete the part in the Z-direction.

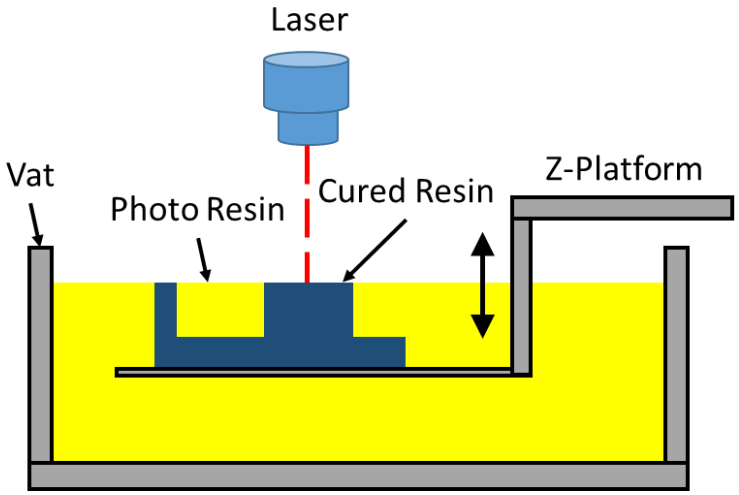

Figure 2.1: Overview of Vat Polymerization Process

The main disadvantage of vat polymerization for RF applications is the inherent material loss of the resin. All UV curable resins, to the best of my knowledge, have a relatively high loss tangent (i.e. >0.01), therefore, making this process unacceptable for low-loss electromagnetic systems.

2.1.2 Material Jetting

Material jetting is similar to vat polymerization in that a UV curable resin is used as the base material. The main difference is that instead of using a large vat of resin the material is "jetted" in small droplets out of a print head, similar to an ink jet printer. Each layer is then cured using UV light and successive 2D layers are combined to create a 3D object. This process is known as photopolymerization. Materials suitable for printing include thermoset polymers. The process is illustrated in the figure below.

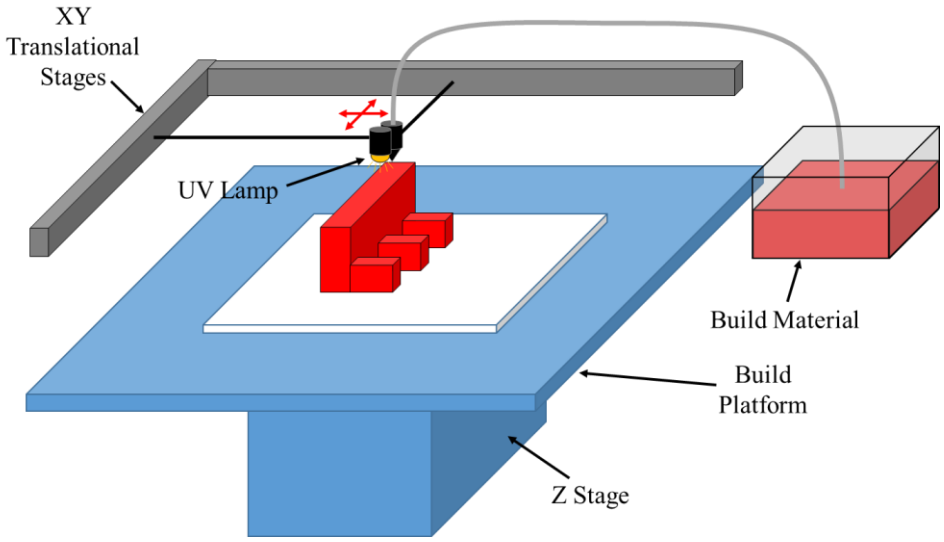

Figure 2.2: Overview of Ink Jetting

Initially, it may appear that ink jetting is a viable solution for RF applications. However, there are some limitations and disadvantages to inkjetting that make it less desirable for some RF applications. First, there is a limited library of materials. In order for a material to be jetted, the viscosity of the material must have a viscosity on the magnitude of water. Unfortunately, highly loaded solutions, especially metals, will not work in the system. Also, the loaded materials must have particle sizes on the nanometer scale. Another limitation is that the thickness of a inkjetted layer is incredibly thin. This makes print times significantly longer compared to FDM, and decreases metallic conductivity since it will print such thin metal layers. Lastly, much like the vat polymerization process, UV curable materials are not ideal for electromagnetic applications unless material loss is not a concern or is desired. Therefore, material jetting is not the ideal method for this applications.

2.1.3 Binder Jetting

This process utilizes two materials to complete the binder jetting process. These materials include a binder and a powder based material. The purpose of the binder is to adhere powder particles together. The printing nozzles are translated on an XY stages and deposits alternating layers of the binding and powder material. Once a layer is complete, the platform is lowered, and a new layer of powder and binder are deposited on top.

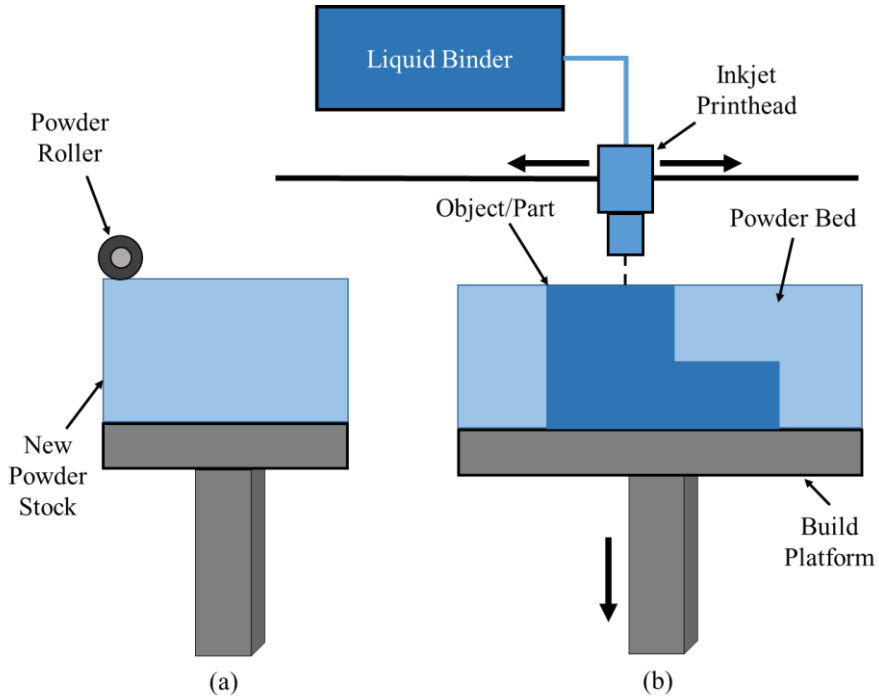

Figure 2.3: Binder Jetting Overview

Because of the binding technique lacks a strong particle to particle bond, materials are not structurally robust. Secondly, the finished parts created by binder jetting have an incredibly high surface roughness. This is due to the binding of powder

particles to form the object. High surface roughness of materials, especially metals, are not suitable for high frequency RF applications. High surface roughness produces unnecessary loss. For these reasons, binder jetting is not the most suitable additive manufacturing technique for fabricating electromagnetic systems.

2.1.4 Material Extrusion

Material extrusions, also commonly known as fuse deposition modelling (FDM), is an incredibly popular additive manufacturing method. Its popularity is to the extent that FDM printers are making their way into peoples' homes as commercially available 3D printing systems. The FDM printing process works by feeding a thermoplastic filament at a constant speed into a heated nozzle. Much like the other processes, the printed part is fabricated layer-by-layer. Adhesion by layers is caused by the hot and liquid thermoplastic being deposited on previous layers of thermoplastic. The liquid thermoplastic exiting the nozzle heats up the previous layer, both layers begin to cool, and form a bond. The previous processes described leveraged UV curable materials. The FDM process does not utilize UV curable materials. It only uses thermoplastics such as ABS, PLA, polycarbonate, and nylon. These materials are relatively low-loss when compared to the UV curable materials used in the AM methods described earlier.

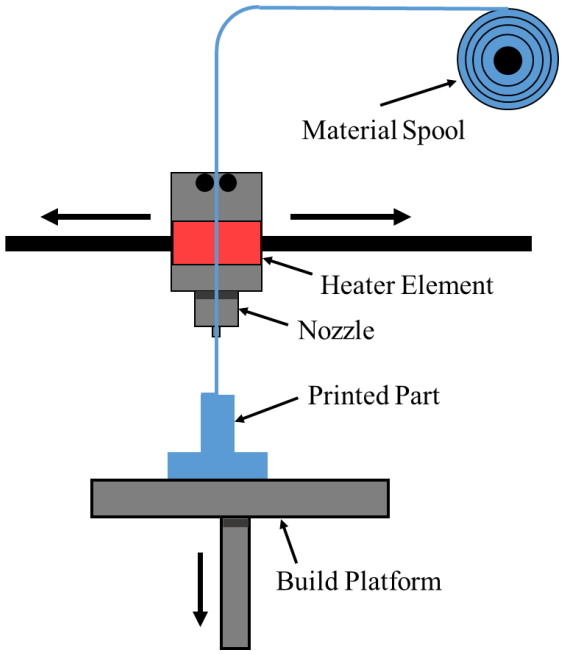

Figure 2.4: Material Extrusion Overview

Due to the low dissipation factor of the thermoplastic materials, FDM appears to be quite suitable for additively manufacturing electromagnetic systems.

2.1.5 Powder Bed Fusion

Powder bed fusion is an umbrella term for various printing methods: selective laser sintering (SLS), selective laser melting (SLM), selective heat sintering (SHS), electron beam melting (EBM), and direct metal laser sintering (DMLS). Figure 2.5 is a general illustration for the various printing methods. All the processes comprise of spreading powder over previous layers. The new powder is supplied by a roller or a blade moving powder from a reservoir. The new powder provides the needed material to add the next layer.

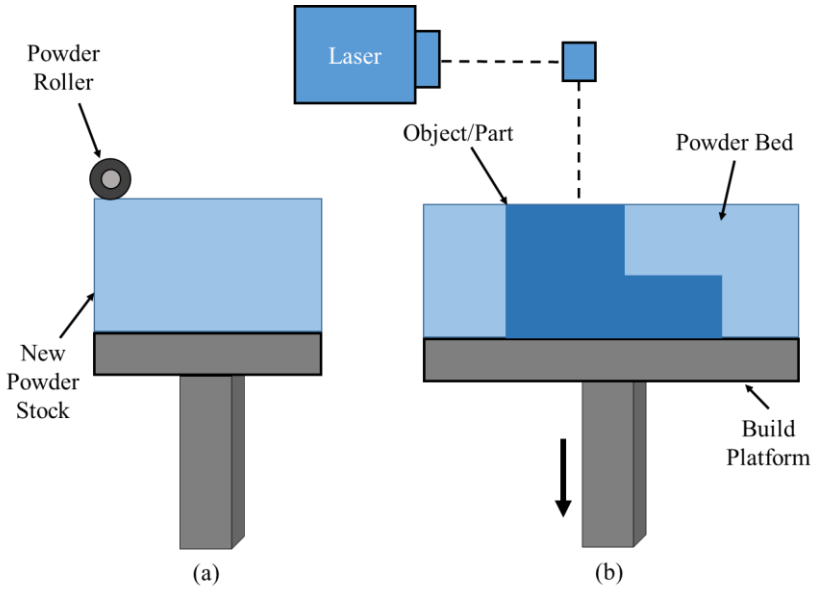

Figure 2.5: Powder Bed Fusion Overview

The major difference between the printing processes is the materials used in the process. DMLS is similar to SLS. However, DMLS uses metals whereas SLS uses plastics, nylons, and ceramics. SLM is when the powder is being melted instead of sintered. EBM places the printing process under a vacuum and uses an electron beam to fuse together metals and alloys to create mechanical parts. SHS is much like the SLS process, but uses a thermal print head to fuse together plastic powder particles. SHS systems are smaller and cheaper compared to SLS systems. SHS achieves this by skipping the laser component and uses a thermal heater.

The combination of these systems provide a way of fabricating plastics and metals. Having a library of dielectric and metals permits the fabrication of electromagnetic systems. As for the plastics, FDM is a much simpler and cheaper AM method for fabricating dielectrics. As for the metals, the metal parts produced by

powder bed fusion are incredibly rough. Metals with high surface roughness are not ideal for RF platforms.

2.2 Materials for Additive Manufacturing RF Applications

In this section, I will be covering a wide range of additive manufacturing materials, their material characteristics, and their suitability for RF applications. The best materials for most RF applications low dielectric losses, high dielectric constants, and high conductivity for the case of metallic materials. These losses can be minimized by targeting dielectric materials with loss tangents and metallic materials with high conductivity. Figure 2.6 illustrates various thermoplastic polymers' dielectric constants and loss tangents.

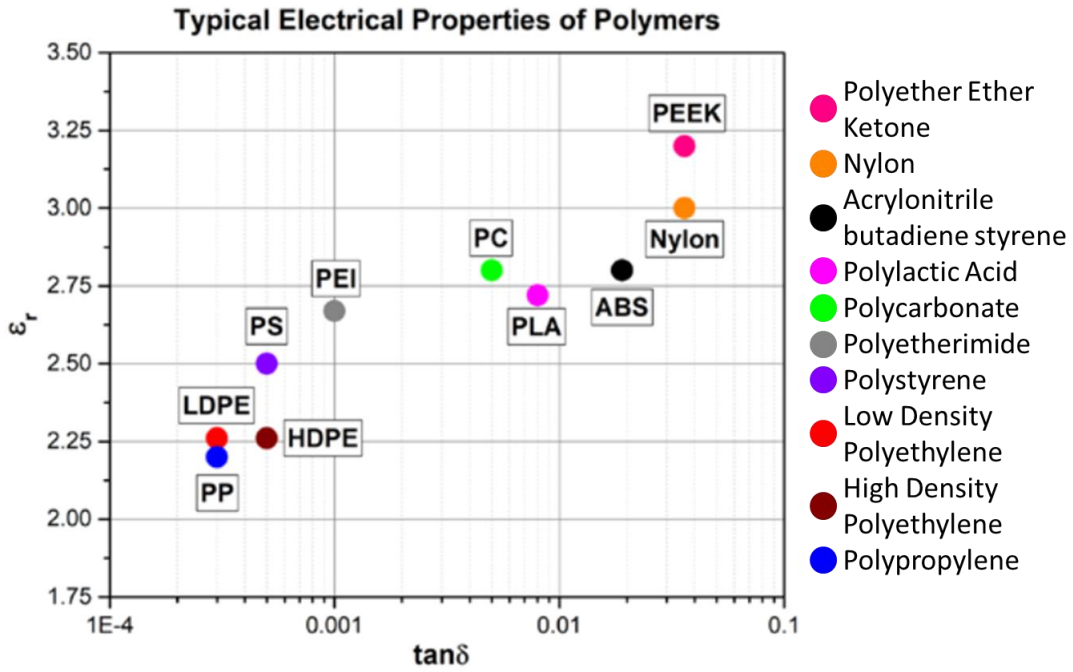

Figure 2.6: Relative permittivity and loss tangent of well-known thermoplastic polymers

I will explore each of these materials in detail and share their suitability for RF applications. In regards to the additive fabrication method, SLA materials are excluded due to the inherently loss nature of the UV curable polymers. Binder jetting and powder bed fusion are excluded due to the high surface roughness of the final part. Therefore, FDM is the best fabrication method for creating dielectrics for RF applications.

Most additively manufactured metals are fabricated through SLS. Unfortunately, the thermoplastic materials will not survive the high energy environments of SLS. For printing of conductive materials I use conductive pastes that are printed via microdispensing or paste extrusion.

2.2.1 Thermoplastic Materials for RF Applications

Figure 2.6 illustrates several common thermoplastics used in FDM printers. As mentioned earlier, low loss dielectric thermoplastics are desirable for RF applications. Therefore, it makes the most sense to target the lower loss tangent materials. Unfortunately, many of the materials with very low loss are difficult to print. Some of these printing hurdles include: bad build plate adhesion, poor layer-to-layer adhesion, and high printing nozzle/build plate temperatures. Table 2.1 characterizes the materials shown in Figure 2.6 in terms of mechanical strength, printing difficulty, printer nozzle temperature, and build plate temperature.

Table 2.1: Thermoplastic robustness, printing difficulty, and print parameters

Thermoplastic	Strength	Print Difficulty	Print Temp.	Bed Temp.
PLA	Low	Low	200C	50C
ABS	Medium	Medium	230C	100C
Nylon	High	Medium	250C	85C

PC	High	Medium	300C	100C
PEI	Very High	Very High	360C	150C
PS	Low	High	240C	115C
HDPE	Low	High	245C	60C
LDPE	Low	High	245C	60C
PP	Low	High	250C	110C

Although, PS, LDPE, HDPE, PEI, and PP have the most attractive loss tangents, the printing difficulty and mechanical strength make them an unattractive material choice. The next best loss tangent available is polycarbonate. Polycarbonate mechanical strength is excellent, the printing difficulty is not challenging, and the printing temperature parameters is achievable by most 3D printers. For these reasons, polycarbonate is the most suitable dielectric material for 3D printed RF systems.

2.2.2 Conductive Materials for RF Applications

There are numerous printable conductive materials available. These printable materials include metal loaded FDM filaments and conductive pastes loaded with metallic flakes. These materials perform sufficiently well at DC but experience obvious conductivity losses above 1 GHz. The highest performing RF printable conductive materials come in silver flake paste and ink forms. A conductivity study was completed to determine the highest RF conductivity for systems operating in the 1-30 GHz range. This is shown in Figures 2.7 and 2.8.

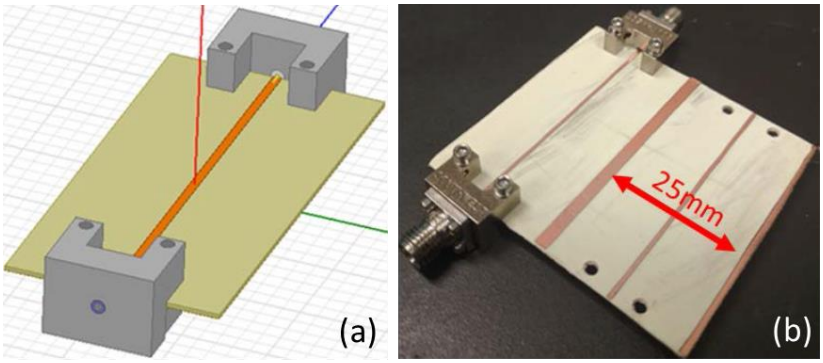

Figure 2.7: Modeled and fabricated copper transmission lines

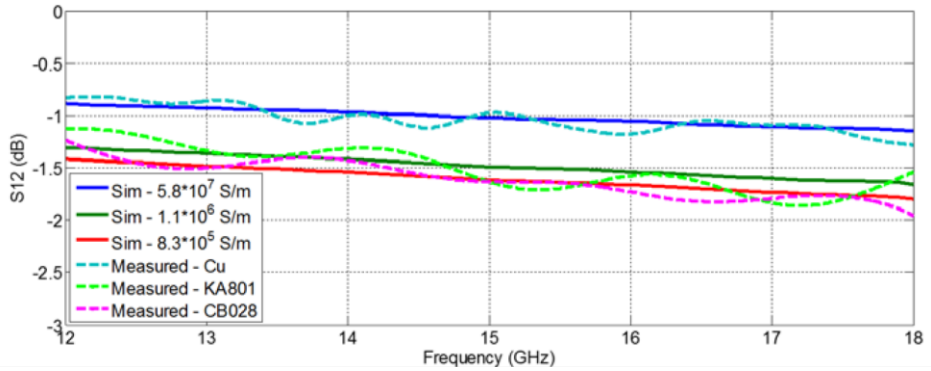

Figure 2.8: Measured and simulated transmission characteristics of printed and copper/baseline microstrip line

There is clearly a performance difference between bulk copper and the other metallic pastes. However, this is expected from a paste with suspended silver flakes. At the conclusion of the study, KA801 was determined the most suitable metallic material.

In this chapter, I provided background the various AM systems and their suitability towards the RF applications of interest in this research. I also summarized

the different base materials that are suitable for 3D printing of RF devices. In the next chapter, I will provide background on passive beamforming.

Chapter 3

BACKGROUND ON PASSIVE BEAMFORMING

In this chapter, I will describe various beamforming methods in addition to the fundamental concepts that enable their beamforming effect. These include: active phased array beam steering, mechanically steered antenna, 2D passive beam steering, and 3D passive beam steering. I will also discuss the pros and cons of each approach.

Active Phased Array Beam Steering: The first method to be discussed is active phased array beam steering. These systems work by applying a varied phase delay to each of the antenna elements that make up the phased array. By changing the phase delay to each antenna, it is possible to scan a high gain beam in various directions (illustrated in Figure 3.1(a)). This technology has given birth to a large range of electrically steerable arrays used for SATCOM, ballistic missile detection/tracking, and other long range communication systems. One large benefit of the phased array approach is that it can obtain very high steering resolution within its field of view. A disadvantage to this method, however, is that the electronic components that make up the entire system can be quite expensive and operation only over a very narrow bandwidth.

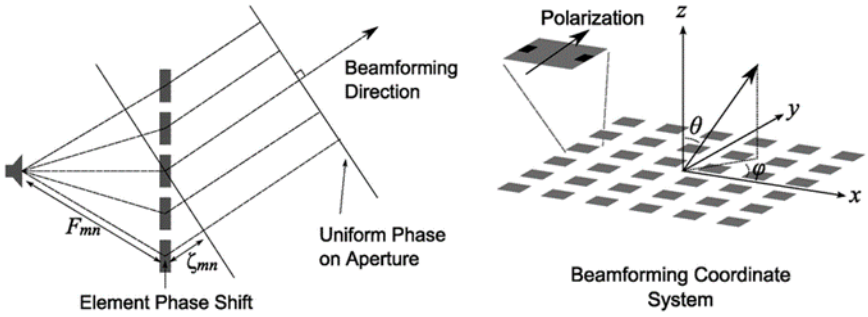

Figure 3.1: Active phased array beam steering overview

Mechanically Steered Antennas: The next beamforming method is mechanically steered antennas. This beamforming technology is incredibly common in satellite communication and low cost radar. Typical mechanically steered antennas are composed of a feed and a reflector antenna. The feed is positioned so that the outgoing waves are at the focal point of the metallic reflector. The reflecting wave is collimated into a plane wave propagating away from the metal reflector. The feed and reflector configuration is illustrated in Figure 3.2. In order to steer the outgoing information, the reflector must be mechanically pivoted. For large reflector antennas, this is not a trivial feat. An advantage to the reflector antenna is that is as broadband as your feed. Also, the fabrication and engineering costs are significantly less than active phased array systems of a similar gain performance.

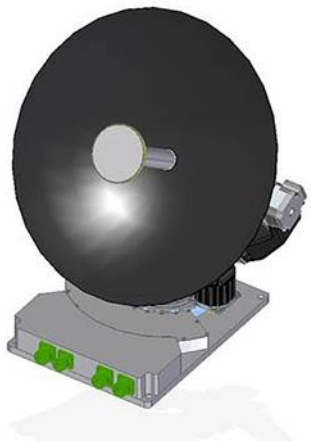

Figure 3.2: Mechanically steered antenna

3D Passive Beam Steering: The third beamforming method is a 3D passive beam steering system. This method leverages a graded refractive index (GRIN) gain enhancement lens such as a Luneburg or Maxwell Fisheye lens. A discrete number of antennas are placed along the backside of the gain enhancing lens. Once an antenna is excited, the power propagates through the lens and outputs a high gain beam on the opposite side of the lens. This relationship is reciprocating: a high gain incident beam will focus on the opposite side of the lens into an antenna. This phenomenon is illustrated in Figure 3.3. This particular system has several distinct advantages: the system is as broadband as your radiating elements, the Luneburg lens can support multiple beams simultaneously, and the entire system is inexpensive. A major disadvantage to this type of beamforming is that the resolution is limited. There are discrete antenna locations on the backside of the lens. Therefore, the system has a discrete number of directions of visibility.

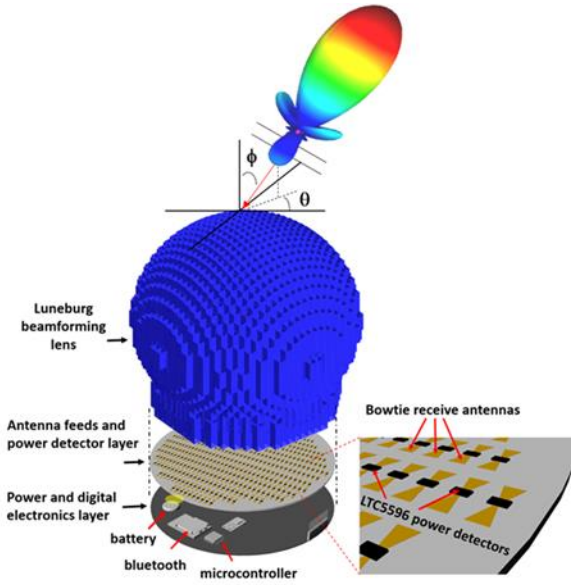

Figure 3.3: 3D passive beam steering

2D Passive Beam Steering: The fourth beamforming technique is 2D passive beam steering. This operates much like the 3D passive beamforming method but only provides gain in one dimension (azimuth or elevation). The Rotman lens is an example of this (shown in Figure 3.4). Each beam port is excited one at a time, the lens introduces the appropriate phase delays to the array ports, and the array ports feed the radiating elements for beamforming. To change the direction of beam steering, another beam port is excited. The 2D passive beam steering system has a few notable properties: it supports multiple beams without needing active phase shifters and is very broadband. A few disadvantages are that it provides gain in only either the azimuth or elevation plane. Also, there are a discrete number of excitation positions. Therefore, there are a discrete number of directional beams that can be formed.

The research explored during this thesis involved both 2D and 3D passive beam steering. More detailed descriptions of these methods are provided below.

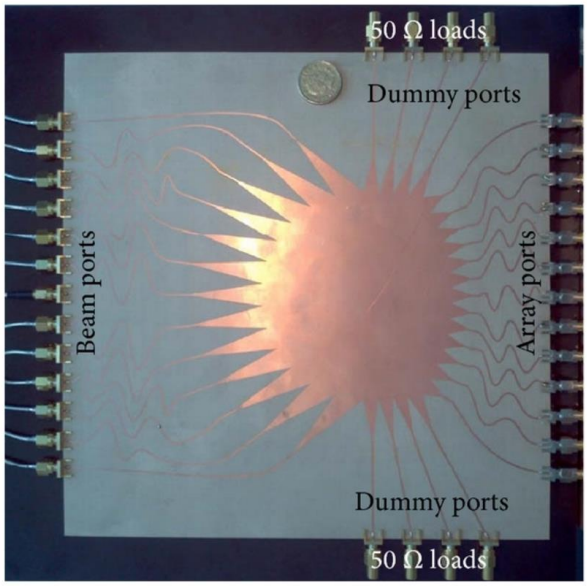

Figure 3.4: 2D passive beam steering (Rotman lens)

3.1 2D Passive Beamforming

2D passive beamforming systems provide high gain in either the azimuth or elevation plane but not both. 2D beamforming is used in applications where a larger field of view is needed in one dimension. For example, if communication or detecting/tracking is needed for a terrestrial application, a 2D beamformer would be used to capture the horizon. In academic literature, cylindrical graded refractive index systems are leveraged to create this beamforming effect [16, 20, 21]. There are several papers covering only the modeling and simulation of 2D passive beamforming. This is due to the complexity in fabricating the dielectric distribution required to create the beamforming effect.

There are a few commonly published techniques to achieve passive beamforming systems. The fabrication techniques described in [16-20] have poor mechanical characteristics, and the processes require an immense amount of human

intervention. In Chapter 4, I describe a novel additive manufacturing system and process to fabricate robust graded dielectrics.

3.2 3D Passive Beamforming

3D passive beamforming is used in applications where high gain is needed in specific direction. 3D passive beamforming excels at detecting and pinpointing the exact location of the object of interest. Because of the high gain of the spot size, 3D passive beamforming excels in SATCOM, multi-beam small cell wireless backhaul applications, and alternative to the traditional parabolic dish antenna.

3D passive beamforming has an additional layer complexity compared to 2D passive beamforming. 2D passive beamformer traditionally takes on a cylindrical shape with its dielectric constant varying radially. 3D passive beamformers have a dielectric constant that varies on all three dimensions. Varying a dielectric constant in all three dimensions is not a trivial feat and is very challenging to fabricate through traditional fabrication methods. In this section, I will extensively elaborate on 3D passive beamforming techniques.

3.2.1 3D Passive Beamforming Lenses

Half Maxwell Fish-Eye lens and the Luneburg lens are two common 3D GRIN lenses can be leveraged for improving gain of a low gain antenna system. The Luneburg lens and Maxwell fish-eye lens dielectric constant spatial distribution are as follows:

$$\varepsilon_r = 2 - \left(\frac{r}{R}\right)^2 \tag{3.1}$$

$$\varepsilon_r = \frac{\varepsilon_0}{\left(1+\left(\frac{r}{R}\right)^2\right)^2} \tag{3.2}$$

Assuming ε_0=4, the Maxwell Fish-Eye lens requires a maximum dielectric constant value of 4. An FDM printable material near this dielectric constant is not readily commercially with a low loss tangent. Using a lossy dielectric material is not practical for this application space. However, the Luneburg lens equation calls for a maximum dielectric constant of 2.0 and a minimum of 1.0. Polycarbonate has a low loss tangent (tanδ≈0.001) and a dielectric constant of 2.68. As described later by slicing the 3D Luneburg lens into subwavelength voxels and leveraging space filling curves, it is possible to realize dielectric distribution called for in the Luneburg lens equation.

3.2.2 Luneburg Lens Based Beamforming

A Luneburg lens is a spatially-graded spherical structure in which every point on the surface is the focal point of a plane wave incident from the opposing surface. Its popularity for antenna applications stems from its broadband nature, potential for high gain, and its ability to form multiple beams.

The original Luneburg lens has a relative permittivity distribution given by

$$\varepsilon_r(r) = 2 - \left(\frac{r}{R}\right)^2 \tag{3.3}$$

where r is the radial distance from the center of the lens and R denotes the sphere radius The lens is very broadband, has potential for high gain, and has the ability to create multiple beams in various directions. These are all attractive characteristics of a directional wireless communication system.

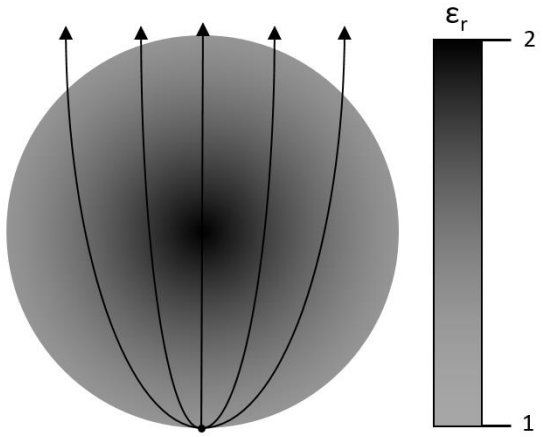

Figure 3.5: Relative Permittivity Distribution of the Luneburg Lens

The Luneburg lens can be manufactured at low cost through FDM. Fabricating a 3D GRIN of this nature is not practical using conventional manufacturing methods. However, investigators at the University of Delaware have developed the methodology to fabricate these dielectric distributions with low cost, high precision, and reproducible results. By utilizing fused-deposition modeling (FDM), I can create the effective dielectric distribution of the Luneburg lens. This is accomplished by utilizing space-filling curves to create subwavelength voxels made up of a thermoplastic polymer and air. By varying the volume fraction of the thermoplastic polymer and air, I can create any desired effective dielectric constant between the upper limits of the polymer ($\varepsilon r \geq 2.0$) and lower limit of air ($\varepsilon_r = 1.0$) within each voxel.

Extensive work has been performed at the University of Delaware on the design and fabrication of Luneburg lenses. Lenses have been fabricated for X, Ka, and W bands. Secondly, several studies were performed on the relationship between lens size and gain. Lastly, simulations were completed to show that various radiators

(dipoles, bowtie antennas, slot radiators, and patch antennas) can be used in conjunction with the lens to produce a desired radiation polarization with very high gain.

The Luneburg lens antenna is worth investigating as a 3D passive beamformer. First, the antenna beam can be steered by simply electrically switching or moving the radiating element. Due to the Luneburg lens' spherical geometry, an excitation can be placed anywhere on the surface of the lens. This adds a degree of freedom in the application space, as there are no limitations on which direction one can communicate. For a dish antenna, the antenna needs to be physically moved to redirect its beam. For an antenna of a larger size, this can require a significant amount of power. Secondly, the weight of the communication system will be significantly reduced by using lightweight polymers to fabricate the dielectric distribution of a Luneburg. These materials, particularly polycarbonate, have a much lower density ($\rho = 1.20$ g·cm-3) compared to metals ($\rho \approx 2.70$ g·cm-3) or fiberglass composites ($\rho \approx 1.66$ g·cm-3) used in the dish antenna communication system. Lastly, the cost of the system can be reduced by using an FDM fabricated Luneburg lens. The cost to fabricate a Luneburg lens through FDM is driven by the cost of materials. An in-depth analysis of cost will be described in Chapter 3.2.2.3. These advantages appear very promising. However, there are limitations in the fabrication process that will be described. I will go into detail about these challenges and the performance compromises that will come with it.

3.2.2.1 Lens Size and Gain Relationship

Much like a parabolic dish antenna, the Luneburg lens' gain has a positive correlation with its aperture size. The equation for gain of a parabolic antenna is

$$G_{parabolicdish} = 20 \cdot \log_{10}(\varepsilon_{eff}) + 20 \cdot \log_{10}(\pi \frac{d}{\lambda}) \quad dBi \tag{3.4}$$

where d is the dish diameter, λ denotes the operational wavelength and ε_{ff} denotes the aperture efficiency and is a constant between 0 and 1. For a Luneburg lens antenna, the relationship between gain and normalized aperture size should take on a similar trend. Using HFSS finite element modelling, I have determined a relationship between the realizable gain, operational wavelength, and aperture size. Due to computational limitations, I was only able to simulate lenses with diameters less than 15 times the operational wavelength. This translates into a lens antenna with a maximum gain of 29 dBi. However, using the data up to 29 dBi and the known dependence on the aperture size I was able to extrapolate to larger Luneburg aperture sizes and higher gain values using a least squares fit. These projections and least squares fit equation are presented in Figure 3.6 and Equation 3.5.

$$G_{Luneburg} = -3.3 + 20 \cdot \log_{10}(\pi \frac{d}{\lambda}) \quad dBi \tag{3.5}$$

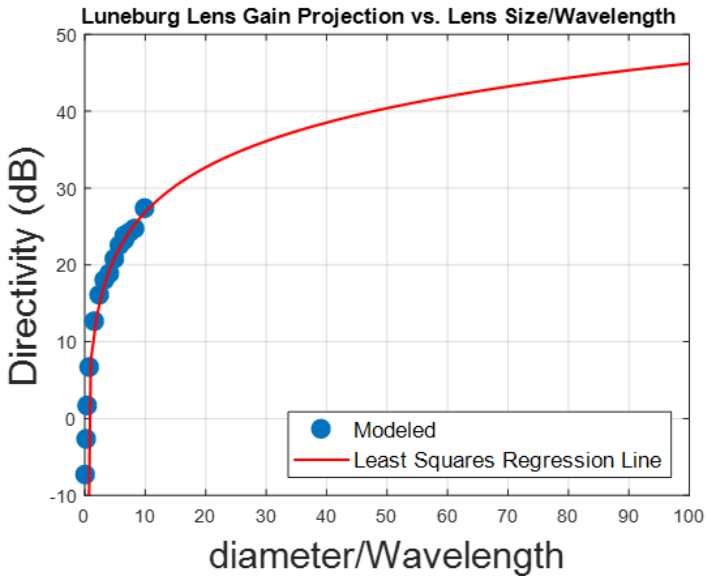

Figure 3.6: Luneburg Lens Gain Projection

Figure 3.6 uses the previous data to demonstrate how large a lens would need to be at a certain frequency to achieve a desired gain.

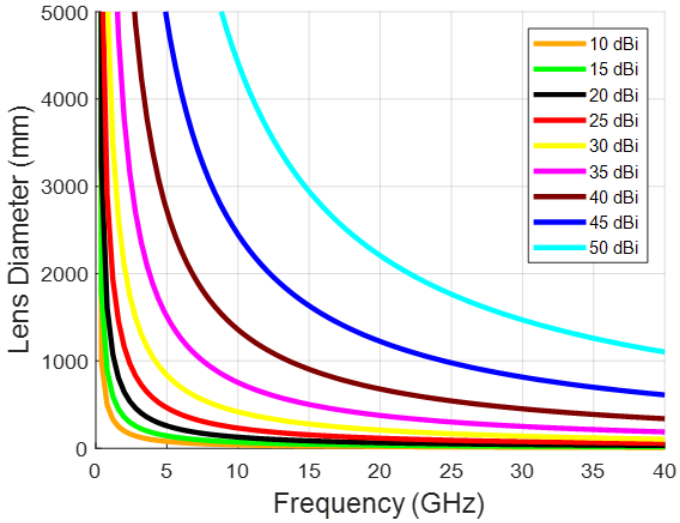

Figure 3.7: Lens Diameter Projection at Constant Gains

Using Figures 3.6 to 3.7, it is obvious that the Luneburg lens would need to be very large across all frequency spectrums (C, X, Ku, and Ka) to achieve gain values approaching 50 dBi. Fabricating lenses of a few meter in size is not a trivial feat, as many FDM printing platforms do not support this size of print volume. Secondly, a high-resolution print of this size could realistically take several weeks to fabricate. Unfortunately, an FDM printing approach is not a viable option to fabricate a lens to operate at all frequency bands (particularly HF to C band).

3.2.2.2 Radiating Feed Elements

The Luneburg lens can be used in conjunction with any low gain radiating element. When a low gain radiating element is abutted along the outer edge of a Luneburg lens, the lens outputs a higher gain beam. The relationship is also reciprocating. When a high gain beam is incident upon the lens, the output is a low gain signal. This reciprocating relationship allows the Luneburg lens to be used for both transmitting and receiving platforms.

The polarization at the output of the Luneburg lens is controlled by the polarization of the radiating element. The following radiating elements have been designed and simulated to show they can be used to excite a Luneburg lens: waveguide, microstrip fed slot antenna, dipole antenna, bowtie antenna, patch (including corner fed and corner cut for CP) antenna. Table 3.1 shows features of each radiating element.

Table 3.1: Radiating Elements

Antenna	Broadband	Peak Directivity	Polarization

Open Ended Waveguide	Yes	5.5-7.8 dBi	Linear
Slot Antenna	No	5.2 dBi	Linear
Dipole Antenna	No	1.75-2.25 dBi	Linear
Bowtie Antenna	Yes	6 dBi	Linear
Patch Antenna	No	8-9 dBi	Linear
Corner Fed/Corner Cut Patch Antenna	No	8-9 dBi	Circular

The radiating elements shown in Table 3.1 have been simulated in HFSS to shows that they can be used with the Luneburg lens to produce a high gain beam. The directivities listed in the Table 3.1 are without the enhancement from the Luneburg lens. However, when the Luneburg lens is placed in front of the radiating element, the outputted gain follows the projections shown in Figure 3.6.

3.2.2.3 Size, Cost, Weight and Power Handling Analysis of Lens Fabrication

In this section, the size, cost, and weight projections will be covered in detail. These projections can be realized through mathematical analysis, where several parameters are needed to formulate a reasonable projection. First, I need a volume fraction relationship between the effective relative permittivity of my dielectric polymer and air. This relationship will allow us to diagnose a specified dielectric constant at every location in the spherical Luneburg lens. This allows the design of the lens' relative permittivity as a function of radius, where this relation is well documented in scientific literature. Second, the mass density of the chosen polymer to estimate the weight of the lens. Third, the cost of the polymer by mass ($/kg) to estimate the materials cost of the completed lens. With this information, projections on size, weight, and cost can be calculated.

I used polycarbonate to additively manufacture a Luneburg lens. This was achieved by using fill fractions of polycarbonate and air to spatially vary the effective permittivity as described in the next section.

Polycarbonate was chosen for its low loss tangent and its ease to print via FDM. The effective dielectric permittivity projections based on volume fraction can used to determine the size, weight, and cost of a lens of an arbitrary diameter. The rest of this section will describe the calculations that can be used to project size, weight, and cost.

The relationship between effective permittivity and volume fraction is linear in the transverse orientation. This relationship can be characterized by Equation 3.7, where vf is the volume fraction of polymer and $\varepsilon_r(vf)$ is the effective relative permittivity of a given volume fraction.

$$\varepsilon_r(vf) = 1.65(vf) + 1 \tag{3.7}$$

The Luneburg lens dielectric distribution is used to determine the volume fraction in various locations of the lens. R is the maximum radius of a given lens and r is any radius within the lens.

$$\varepsilon_r(r) = 2 - \left(\frac{r}{R}\right)^2 \tag{3.8}$$

Insert Equation 3.7 into Equation 3.8 to solve for the volume fraction of polymer to air to determine required volume fraction at certain radius within the lens. Equation 3.9 is the result.

$$vf(r) = \frac{1-(r/R)^2}{1.65} \tag{3.9}$$

The effective mass density of the polycarbonate and air is a function of the volume fraction of polycarbonate and air. Equation 3.10 shows that relationship, where ρ_{eff} is

the effective mass density of polycarbonate and air, and ρ_{PC} is the bulk mass density of polycarbonate.

$$\rho_{eff} = (vf)(\rho_{PC}) \tag{3.10}$$

Insert Equation 3.9 into Equation 3.10 to solve for the effective mass density as a function of radius of the Luneburg lens. Equation 3.11 is the resulting equation.

$$\rho_{eff}(r) = \rho_{PC}\left(\frac{1}{1.65}\right)\left(1 - \left({}^{r}/_{R}\right)^{2}\right) \tag{3.11}$$

To calculate the mass of a sphere of a radially varying mass density, the following equation is used.

$$M = 4\pi \int_{0}^{R} r^{2}\rho(r)\, dr \tag{3.12}$$

Combining Equations 3.11 and 3.12, I arrive at an expression for the total mass of a Luneburg lens of an arbitrary radius.

$$M = 4\pi\rho_{PC}\left(\frac{1}{1.65}\right)\int_{0}^{R} r^{2}\left(1 - \left({}^{r}/_{R}\right)^{2}\right) dr \tag{3.13}$$

After integration, Equation 3.12 becomes:

$$M = 1.0155(\rho_{PC})R^{3} \tag{3.14}$$

$$M = 0.1269(\rho_{PC})D^{3} \tag{3.15}$$

Equations 3.13 and 3.14 can be used to calculate the total mass of polycarbonate Luneburg lens with an arbitrary radius/diameter. This equation can be used to calculate the cost of fabrication as well. FDM materials are listed as price per weight. Therefore, Equation 3.14 can be multiplied by the cost per weight to calculate the total cost of materials as well. Equation 3.14 can be used to calculate the total cost of material to fabricate the Luneburg lens. The price per kilogram used in this calculation, for polycarbonate, is $100/kg.

$$Cost = M * \left(\frac{price}{weight}\right) \tag{3.16}$$

$$\text{Cost} = 0.1269(\rho_{PC})D^3\left(\frac{\text{price}}{\text{weight}}\right) \tag{3.17}$$

Figures 3.8 and 3.9 plot the cost and weight as a function of lens diameter.

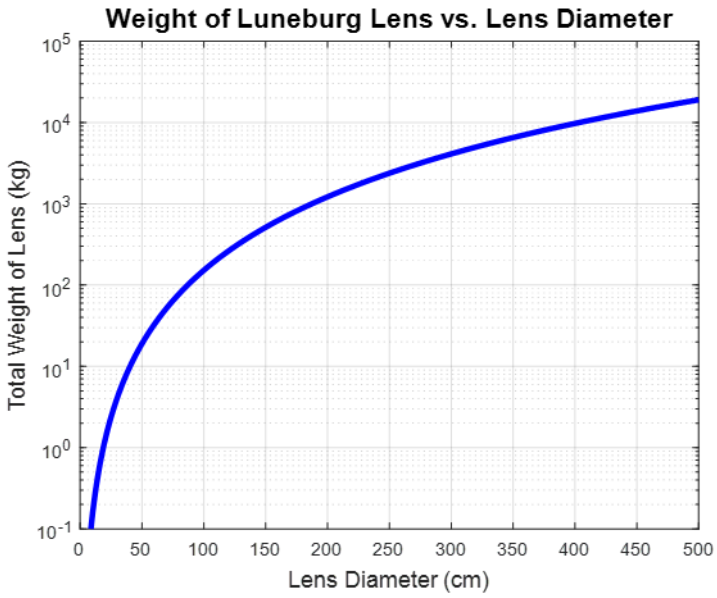

Figure 3.8: Luneburg Lens Weight Projection

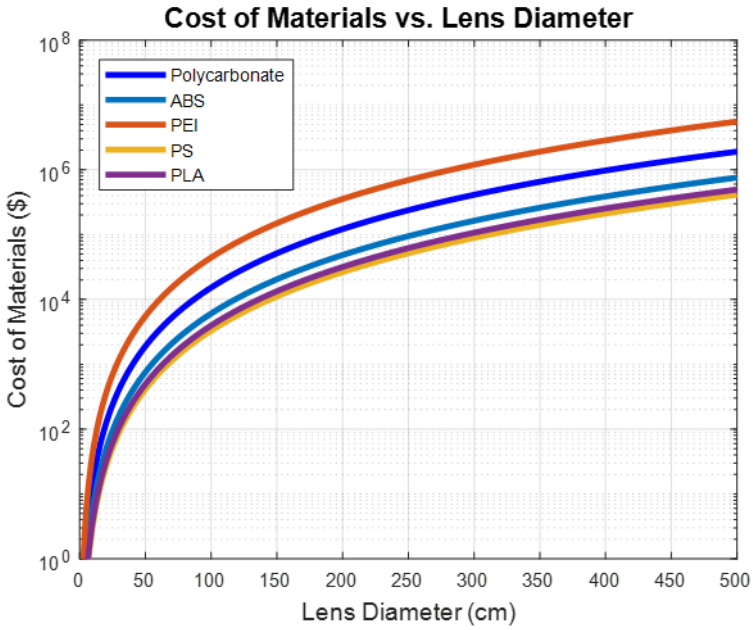

Figure 3.9: Luneburg Lens Cost Projection

According to Figures 3.8 and 3.9, fabrication of a small lens (<30 cm) is very lightweight and inexpensive. However, as the diameter of the lens increases, the weight and cost figures increase at a rapid rate. Also, a majority of additive manufacturing systems do not support build volumes greater than 30 cm in each dimension. A much larger printing system will be needed to produce a larger lens. If a print job exceeds a print volume, it is possible to print the lens in sections and bind each section together.

A power handling study was done to understand how much power will dissipate in the polymer used for beamforming. Fortunately, due to polycarbonate's bulk low loss tangent (~0.002), the power handling allows a large amount of power to pass through the lens. Energy dissipated in the polycarbonate becomes a concern when the material approaches the glass transition temperature (147 C). As this occurs, the

material robustness is compromised. However, this will only occur when an immense amount of power is incident on the lens for an extended period of time.

A study was done in HFSS to better understand how much power will dissipate within the lens. Below, in Figure 3.10, shows the power dissipation density of a lens (d = 130 mm) with 3 MW input power.

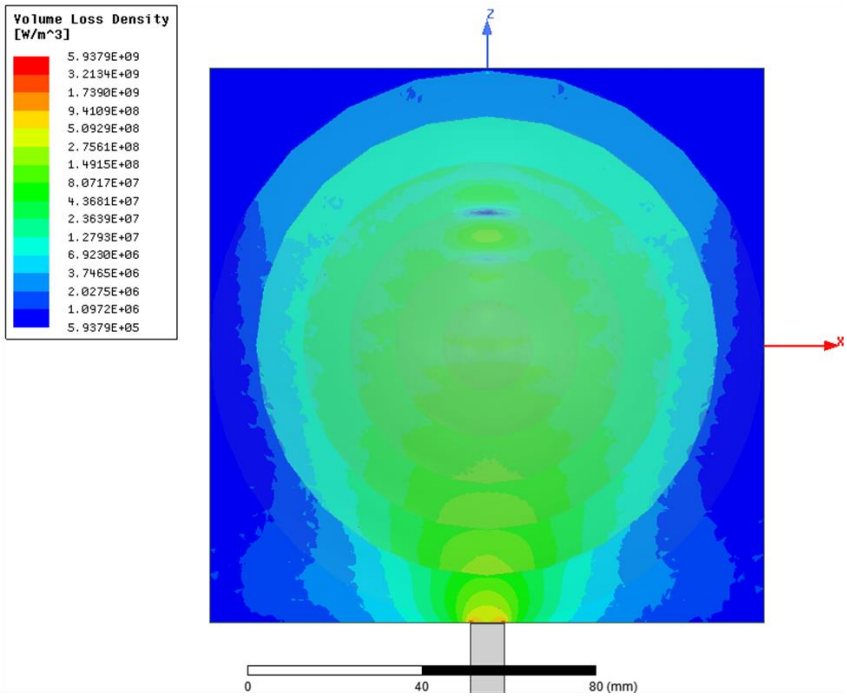

Figure 3.10: Volume Loss Density of Luneburg Lens (d = 130 mm @ 18 GHz)

Using Table 3.2, it is possible to simulate how much power is dissipated throughout the lens at each of the frequency bands for various lens sizes. The power dissipated in the lens is a linear function of incident power. The values in Table 3.2 are normalized and can be used to predict dissipated power using an arbitrary incident power.

Table 3.2: Percentage Power Loss of Various Lens Diameters

Frequency Band	Lens Diameter	Power Loss (%)
C-Band	50 mm	0.95%
	100 mm	2.48%
	150 mm	3.67%
	200 mm	4.23%
	250 mm	4.95%
X-Band	50 mm	1.22%
	100 mm	4.13%
	150 mm	5.50%
Ku-Band	20 mm	1.17%
	30 mm	1.72%
	40 mm	2.20%
	50 mm	3.34%
	100 mm	4.33%
Ka-Band	10 mm	1.09%
	15 mm	2.71%
	30 mm	4.70%
	45 mm	5.25%
	60 mm	5.27%

Chapter 4

2D PASSIVE BEAMFORMER IN STRUCTURAL COMPOSITES

4.1 Dry Powder Printing

This chapter describes a custom-made 3D powder printer I developed. Using this printer, I will demonstrate how I was able to additively manufacture a 2D passive beamforming system within a structural composite.

4.1.1 Introduction

The ability to control electromagnetic wave propagation using a spatially varying or graded index of refraction (GRIN) has resulted in a number of practical photonic devices (e.g., GRIN lenses and graded index optical fibers). At microwave frequencies, GRIN structures have also been explored for their use as lens antennas [21], antireflective surfaces [22], and passive beam formers [20]. However, fabricating practical GRIN structures can be challenging. One popular technique is subtractive manufacturing. This method utilizes computer numerical control (CNC) milling to create spatially varying air voids within a solid homogenous dielectric. Assuming the void size and spacing are much smaller than the wavelength, the combination of air pockets and background create a locally varying effective permittivity. Unfortunately, for many applications, drilling air pockets into a substrate significantly compromises the structural integrity of the device.

Thus, it is much more attractive to employ additive manufacturing methods. To this end, I have designed and built a 3D printer that dispenses dry high permittivity

powders between layers of a structural composite to create graded dielectrics [23]. It has been shown [23] that this approach has only a small effect on the mechanical strength of the structural composite. However, this fabrication process results in a permittivity distribution that is anisotropic with different values in the xy-plane (i.e., transverse plane) and along the z-axis (i.e., longitudinal axis). In this study, I examine the full permittivity tensor produced by this additive manufacturing process and validate these properties experimentally. I also provide an effective media model that can be used to predict the anisotropic properties as a function of materials and print parameters. Lastly, I provide a practical illustrative example: Luneburg based passive beamformer.

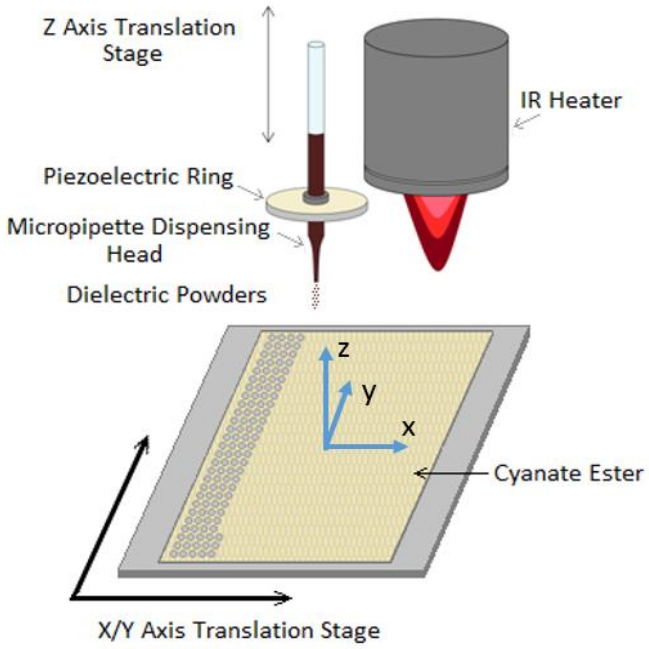

Figure 4.1: 3D powder printing system

4.1.2 3D Powder Printer

A custom 3D powder printer (illustrated in Figure 4.1) was developed to create multifunctional structures with integrated electromagnetic properties. The dielectric properties are manipulated by dispensing a high permittivity powder (Emerson & Cuming's HiK) [24] onto a low-loss woven fabric based composite prepreg material (BTCy-1 6781 by TenCate) [25]. A spatially varying powder distribution is realized by moving an electrically controlled power valve over the surface of the composite substrate. At any specific location, the ratio of dispensed powder to surface area defines the local effective permittivity.

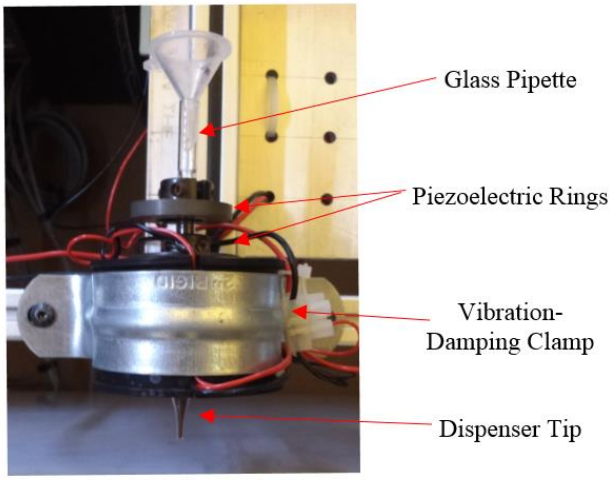

Figure 4.2: Close up of dispensing unit.

To dispense the dry powder in a desired pattern, I used a powder "valve" deposition system (Figure 4.2). The design of this dispensing system, composed of a glass pipette and bonded piezoelectric ring, was originally described by Yang [26-32]. The diameter of the pipette opening must be small enough that powder does not

dispense under static conditions (no vibrations delivered by the piezoelectric ring). Specifically, this requires the pipette orifice to be approximately 5 to 6 particle diameters at its tip. To initiate powder flow, an AC voltage (~10 Volts peak-to-peak) is applied to the piezoelectric ring. This causes the pipette to vibrate at a reasonably high frequency (42 kHz) causing the powder to freely flow out of the orifice of the pipette. The frequency of vibration was determined experimentally to optimize effective powder flow for Emerson & Cuming's HiK powder. The powder flow then stops once the AC signal is toggled off. Figure 4.3 illustrates this effect through time-lapse photographs. The powder that flows out of the pipette lands on the substrate and forms a small dot. The size of the pipette orifice and the duration of the electrical pulse determine the amount of powder dispensed. I typically used an average powder dot size of 2.0-2.5 mm diameter. This is equivalent to approximately 2 milligrams of powder.

The first layer of prepreg is taped to the xy-stage. The powder printer is then used to print the powder distribution on that first layer. An infrared heater scans over the surface to heat the substrate, so that the powder adheres. The user then manually places a new prepreg substrate layer on top and repeats the process. Since the xy-stage maintains its last position under computer control each printed layer is fully registered to the previous layers (this is how print alignment is ensured). After all layers are printed, the entire stack is post-processed in the autoclave.

The autoclaving process is needed to cure the impregnated resin, bind stacking substrates together, and remove unwanted air pockets. This is achieved by utilizing high pressure (50 PSI) and temperature (350^{o}F). As the temperature ramps up in the autoclave chamber, the resin of the composite prepreg becomes less viscous and

begins to flow. A caul plate, placed on top of the printed system, forces excess resin to move laterally and creates a uniform thickness throughout the part. The pressure also forces the fibers to nestle together better. The vacuum removes unwanted air pockets during this process. As the chamber temperature nears 350^{o}F, the curing process of the resin is further catalyzed. The combination of neatly nestled fibers and cured resin contributes to the robustness of the system.

The thickness is driven by the number of prepreg composite layers and the amount of powder dispensed. The final product is a structurally robust plate with a permanent distribution of powder creating integrated dielectric properties. Figure 4.4 summarizes the entire process.

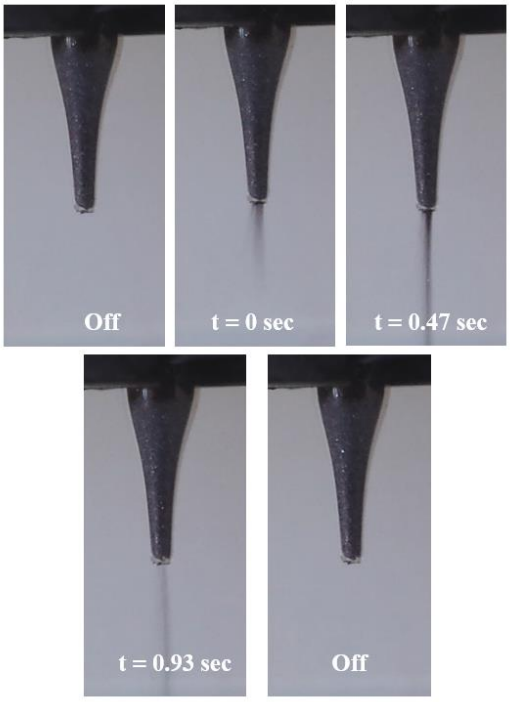

Figure 4.3: Time lapse photographs of the powder dispensing tip.

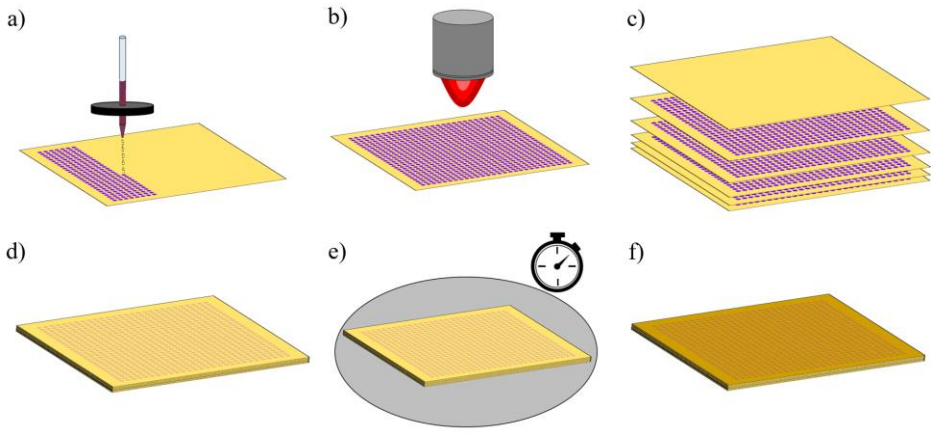

Figure 4.4: Timeline of the 3D printing process: a) powder is dispensed onto the composite substrate in a desired pattern, b) an IR heater is used to soften the impregnated resin so that the powder adheres to the substrate, c/d) all printed layers are aligned and stacked, e) an autoclave is used to cure the resin and bind the stacked layers, and f) the end result is a robust part with embedded spatially varying dielectric properties.

4.1.3 Material Selection

Three main criteria were considered for selecting materials for this system: mechanical resiliency, a low loss tangent, and a high dielectric constant contrast between dispensed powder and substrate.

The substrate that was chosen was an S-glass/cyanate ester fiber reinforced composite prepreg (BTCy-1 sold by TenCate). This material has desirable mechanical properties and a low microwave loss tangent.

Table 4.1: Table 1: Dielectric properties of used materials measured at 10 GHz.

Material	Dielectric Constant	Loss Tangent
BTC-1 Composite Substrate	4.2	0.003
Emerson & Cuming's HiK Powder	12.0	0.0007

The dispensed material was ECCOSTOCK® HiK Powder. This HiK ceramic powder was chosen for its relatively high dielectric constant, low loss tangent, and relatively large particle sizes (~100 μm). These large particles are well suited for the powder dispensing apparatus discussed earlier.

4.1.4 Effective Media Model

In this section, I provide a model that predicts the effective dielectric properties of the printed samples as a function of the constituent properties of the base materials and the print geometry. Figure 4.5 presents a micro-CT scan of a small portion of a printed sample, illustrating how the HiK powder distributes itself between substrate layers. In this case, a single dot of powder was printed on each of eight stacked layers of composite prepreg. The image is a cross sectional view cut through the center of the "dot stack." I used this "dot stack" configuration to construct the geometries used for my effective media model.

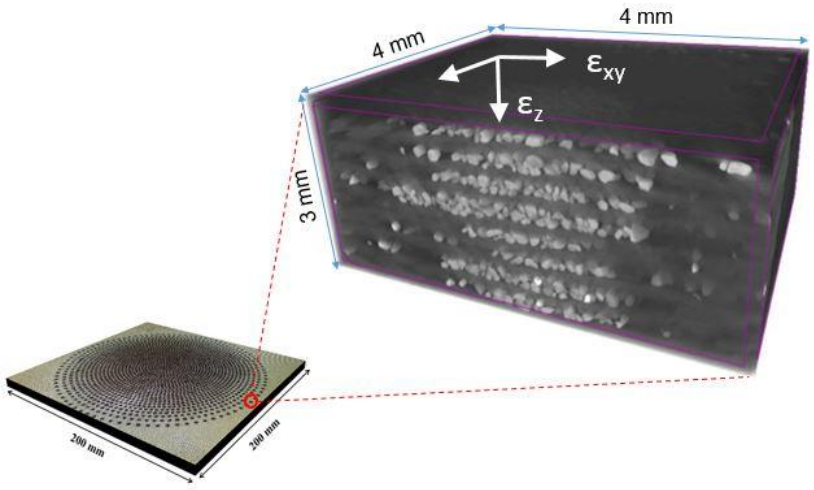

Figure 4.5: Micro-CT image of a portion of a printed sample.

I note that the asymmetry seen in the figure suggests that the dielectric properties are anisotropic with the properties in the transverse xy-plane differing from those along the longitudinal z-axis. I also note that since the powder particle size (~100μm) and the spacing between dots are much smaller than the effective wavelength at microwave frequencies, the electromagnetic properties can be approximated through effective media theory. Figure 4.6 illustrates how the materials will be modeled in their effective geometries.

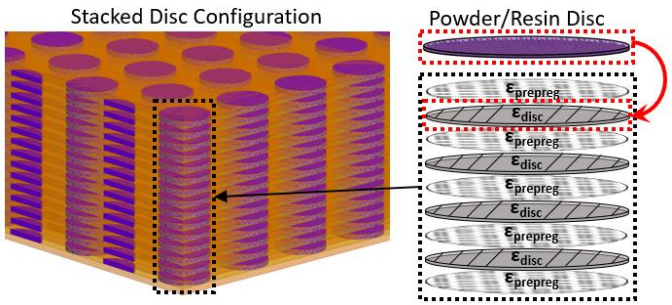

Figure 4.6: Configuration of modeled geometries of printing materials.

My effective media model comprises three main steps. First, the powder disks (i.e., darker regions in Figure 4.6) are modeled as thin disks made of HiK powder and the polymer resin. Second, these disks are stacked vertically between layers of prepreg composite (i.e., background material in Figure 4.6) creating infinitely tall inhomogeneous cylinders. Third, these cylinders are packed in the transverse plane in a periodic array. These three modeling configurations are combined to predict the effective dielectric constant of a printed material system based on local powder density in mg/mm^2. Each of these three steps in the effective media model is presented below.

4.1.4.1 Powder and Resin Disks

A Bruggeman mixture formula [33] was utilized to determine the effective dielectric constant of a thin disk that combines the polymer resin and printed powder. Here, the powder particles were modeled as spheres and the background material was the polymer resin. The effective dielectric properties of the powder/resin composite were then determined using

$$1 - f_{powder} = \frac{\varepsilon_{powder} - \varepsilon_{eff}^{disk}}{\varepsilon_{powder} - \varepsilon_{resin}} \left(\frac{\varepsilon_{resin}}{\varepsilon_{eff}^{disk}} \right)^{1/3} \quad (4.1)$$

where f_{powder} is the volume fraction of HiK powder particles within the disk, ε_{powder} and ε_{resin} are the bulk permittivity of the powder particles and polymer resin, respectively, and ε_{eff}^{disk} is the effective permittivity of the disk. The specific values used to solve for ε_{eff}^{disk} are shown in Table 2.

Table 4.2: Values used in Bruggeman mixture formula

ε_{resin}	2.7
ε_{powder}	12.0
f_{powder}	0.95

For these calculations, I used vendor supplied values for dielectric properties (ε_{resin}=2.7, ε_{powder}=12.0) and a volume fraction of f_{powder} = 0.95. The powder volume fraction was determined by image processing the micro-CT images. This resulted in an effective permittivity ε_{eff}^{disk} of 11.25.

4.1.4.2 Stacked Disks

The next step was to combine the powder/resin disks with the alternating layers of composite prepreg, as illustrated in Figure 4.7. This results in infinitely tall

cylinders of alternating layers of material; a geometry that produces anisotropic dielectric properties.

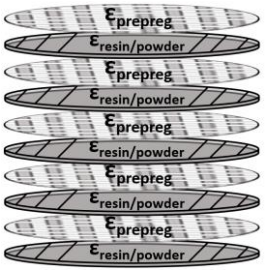

Figure 4.7: Configuration of resin/powder and prepreg disks

The effective anisotropic permittivity for the alternately stacked disks, shown in Figure 4.7, was calculated using a Maxwell-Garnet mixture formula [34]. The specific mixture formulas are given by

$$\varepsilon_{eff,t}^{cylinder} = \varepsilon_h + \varepsilon_h f_{disk} \frac{\varepsilon_{eff,t}^{cylinder} - \varepsilon_h}{\varepsilon_h + (1 - f_{disk}) N_t (\varepsilon_{eff}^{disk} - \varepsilon_h)} \tag{4.2}$$

$$\varepsilon_{eff,z}^{cylinder} = \varepsilon_h + \varepsilon_h f_{disk} \frac{\varepsilon_{eff}^{disk} - \varepsilon_h}{\varepsilon_h + (1 - f_{disk}) N_z (\varepsilon_{eff}^{disk} - \varepsilon_h)} \tag{4.3}$$

where $\varepsilon_{eff,t}^{cylinder}$ and $\varepsilon_{eff,z}^{cylinder}$ are the effective transverse and longitudinal relative permittivities, respectively, of the stacked cylinders, ε_h represents the dielectric properties of the host (prepreg), ε_{eff}^{disk} represents the dielectric properties of the inclusions (powder/resin disk) given by Equation (4.1), f_{disk} is the volumetric fill factor of powder disks to the total cylinder volume, and N_t and N_z are the depolarization factors for the transverse and longitudinal directions, respectively. The specific values I used to solve for $\varepsilon_{eff,t}^{cylinder}$ and $\varepsilon_{eff,z}^{cylinder}$ are shown in Table 4.3.

Table 4.3: Values used in the Maxwell-Garnett formulas

ε_h (prepreg composite	4.2
ε_{eff}^{disk} (powder/resin disk)	11.25
f_{disk}	0.6
N_t	0
N_z	1

The volume fraction of the powder disk, f_{disk}, was determined from micro-CT images. With these values, I calculated $\varepsilon_{eff,t}^{cylinder}$ and $\varepsilon_{eff,z}^{cylinder}$ to be 8.47 and 6.83, respectively.

4.1.4.3 Packed Cylinders

The final step was to determine the effective permittivity of the entire material system by hexagonally packing the infinite cylinders in the transverse xy-plane (as depicted in Figure 4.8). The final effective properties were determined by again employing Maxwell-Garnet mixture formulas given by

$$\varepsilon_{eff,t} = \varepsilon_h + \varepsilon_h f_{cyl} \frac{\varepsilon_{eff,t}^{cylinder} - \varepsilon_h}{\varepsilon_h + (1 - f_{cyl}) N_t (\varepsilon_{eff,t}^{cylinder} - \varepsilon_h)} \tag{4.4}$$

$$\varepsilon_{eff,z} = \varepsilon_h + \varepsilon_h f_{cyl} \frac{\varepsilon_{eff,z}^{cylinder} - \varepsilon_h}{\varepsilon_h + (1 - f_{cyl}) N_z (\varepsilon_{eff,z}^{cylinder} - \varepsilon_h)} \tag{4.5}$$

where $\varepsilon_{eff,t}$ and $\varepsilon_{eff,z}$ are the final effective transverse and longitudinal relative permittivities, respectively, ε_h represents the dielectric properties of the host (prepreg), $\varepsilon_{eff,t}^{cylinder}$ and $\varepsilon_{eff,z}^{cylinder}$ represent the effective properties of the inclusions (i.e., stacked cylinders) given by Equations (4.4) and (4.5), f_{cyl} is the volumetric fill factor of cylindrical inclusions when hexagonally packed, and N_t and N_z are the depolarization factors for the transverse and longitudinal directions, respectively.

Table 4.4: Values used in Maxwell-Garnett packed cylinder mixture formulas

ε_h	4.2
$\varepsilon_{eff,t}^{cylinder}$	8.47
$\varepsilon_{eff,z}^{cylinder}$	6.83
N_t	0.5
N_z	0

The specific values I used to solve for $\varepsilon_{eff,t}$ and $\varepsilon_{eff,z}$ are given in Table 4.4. The specific packing arrangement of the cylinders is equivalent to the volume fraction, f_{cyl}, and Figure 4.8 demonstrates how hexagonal packing of the cylinders can be varied. I note that my specific printing method allows us to overlap cylinders, enabling us to generate packing factors greater than that of a standard hexagonally close packing system. The effective dielectric properties for varying packing factors are shown in Figure 4.9.

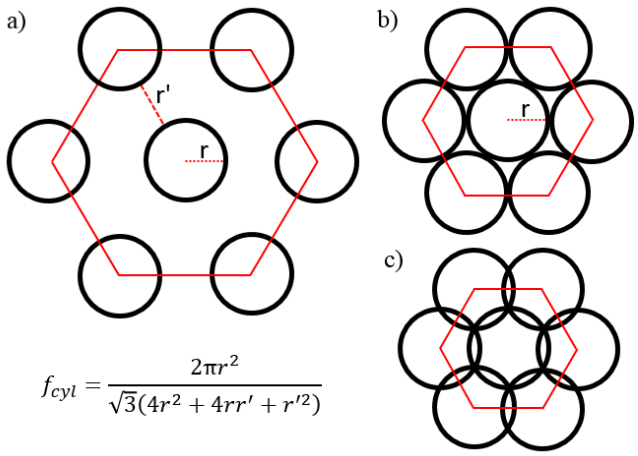

Figure 4.8: Various packing scenarios: a) loosely packed cylinders, b) hexagonally close packing (pf = 0.9069), and c) overlapping cylinders.

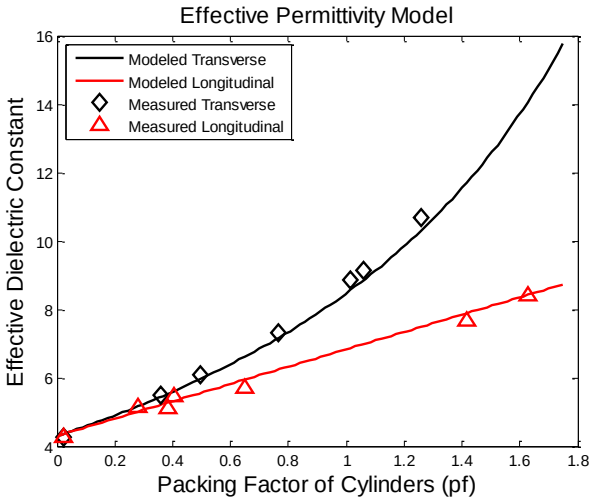

Figure 4.9: Predicted and measured results of effective permittivity of powder printing.

In the next section, I fabricated experimental samples with varying packing factors and determined their transverse and longitudinal permittivities. The model described above was compared to the experimental results (see Figure 4.9) and found to show good agreement. I stress that none of the specific parameters used in the effective media model were varied to fit the predictions to the experimental results. All parameter values either were experimentally measured or were provided by the material vendors.

4.1.5 Experimental Model Validation

I experimentally validated the effective media model by fabricating a number of test samples. I performed two sets of experiments to determine the transverse (ε_{xy}) and longitudinal (ε_z) components of the permittivity tensor,

$$\bar{\bar{\varepsilon}}_{eff} = \begin{bmatrix} \varepsilon_{xy} & 0 & 0 \\ 0 & \varepsilon_{xy} & 0 \\ 0 & 0 & \varepsilon_z \end{bmatrix} \tag{4.6}$$

For the transverse components, I fabricated eight samples of varying powder densities, 0 to 0.51 mg/mm^2 (an example is shown in Figure 4.10). Each sample was a 300 mm x 300 mm x 3 mm uniform plate in which the dot-to-dot spacing was varied while the powder dot weight was kept constant. The mass comparison between dots has reasonably good uniformity. I determined the transverse effective permittivity values (ε_x and ε_y) of each sample by using the focused beam material measurement system described in [23] (Figure 4.11). Over the range of frequencies tested (i.e., 4 GHz to 18 GHz), the maximum dot-to-dot spacing did not exceed 5 mm. This ensured that even at the highest frequency tested, the dot spacing was smaller than the wavelength ($\lambda/3$) and could be treated as an effective permittivity. Results from the seven samples are plotted on Figure 4.13 (black diamond markers) and closely agree with predictions from the effective media model (black line).

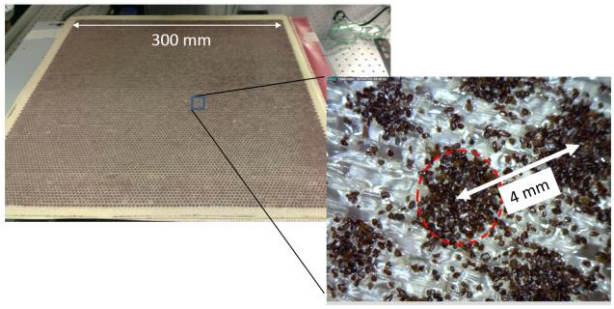

Figure 4.10: Example of a uniform print sample used to calibrate the transverse dielectric properties.

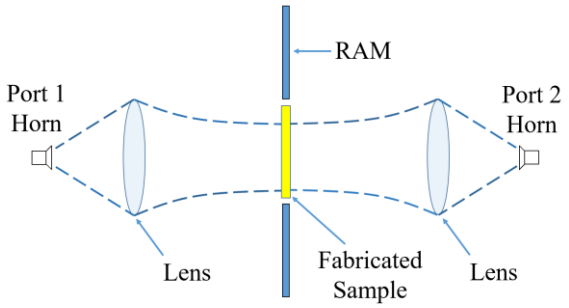

Figure 4.11: Free-space focused beam measurement system.

For the longitudinal component (i.e., ε_z), I utilized a microstrip transmission line method (Figure 4.12a). I fabricated six samples with local powder densities that varied from 0 to 0.66 mg/mm^2 (Figure 4.12b). I used an Agilent E8364 PNA to measure the complex transmission coefficient, S21, over the frequency band of interest. The effective permittivity of the powder printed substrate, $\varepsilon_{substrate}$, was then calculated from the measured effective permittivity of the fundamental microstrip mode, ε_{eff}, using the quasi-static approximations [35] given by

$$\varepsilon_{eff} = \frac{\varepsilon_r+1}{2} + \frac{\varepsilon_r-1}{2}\frac{1}{\sqrt{1+12d/W}} \tag{4.7}$$

$$\varepsilon_{substrate} = \frac{1+(2\varepsilon_{eff}-1)\sqrt{1+12\left(\frac{d}{W}\right)}}{1+\sqrt{1+12\left(\frac{d}{W}\right)}} \tag{4.8}$$

where d is the substrate thickness and W is the width of the metallic microstrip trace (see Figure 4.12a). The effective permittivity was determined directly from measurements using

$$\varepsilon_{eff} = \left(\frac{\partial\phi}{\partial f}\cdot\frac{c}{2\pi l}\right)^2 \tag{4.9}$$

where l is the length of the transmission line, c is the speed of light in a vacuum, and $\frac{\partial\phi}{\partial f}$ denotes the rate of change of the transmitted phase with frequency. Results from

the six samples are plotted on Figure 4.13 (red triangle markers) and closely agree with predictions from the effective media model (red line). From these measurements, I establish a set of calibration curves (Figure 4.13) that predicts the local effective permittivity tensor of the printed samples as a function of the amount of powder dispensed.

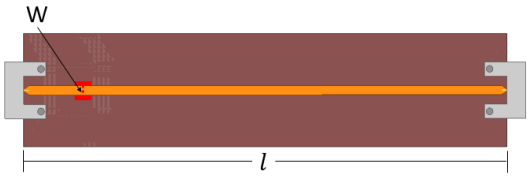

Figure 4.12a:HFSS model of microstrip transmission line on printed composite substrate.

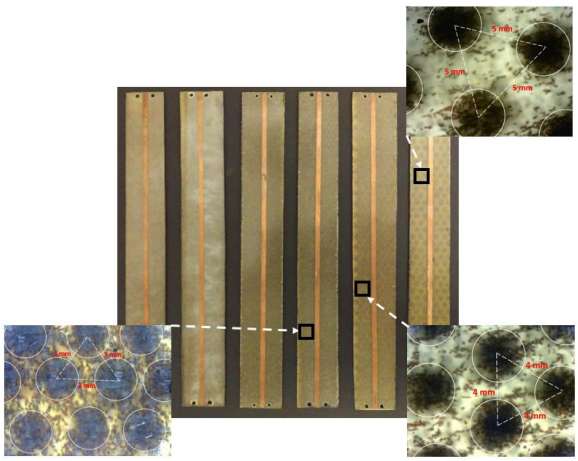

Figure 4.12b:Six calibration samples fabricated using the 3D powder printing system with their effective dielectric constants increasing from right to left. The powder mass per unit area dispensed varied from 0 to 0.66 mg/mm^2. A copper microstrip transmission line was formed on all the samples to measure the in-plane effective permittivity as a function of powder density. Insets show higher magnification of squares outlined in center image. Circles show powder dots and dashed lines indicate dot center-to-center distances.

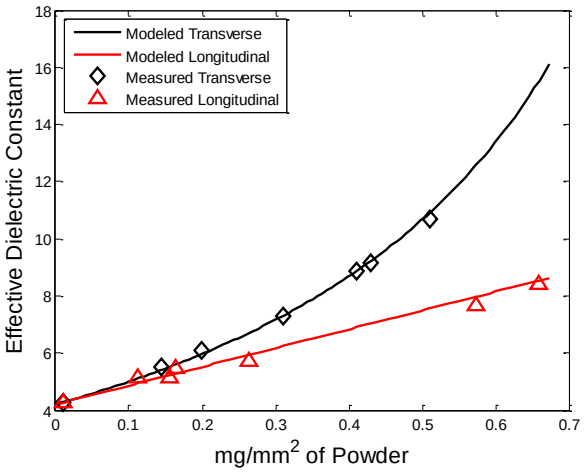

Figure 4.13: Calibration curves that relate transverse and longitudinal permittivity to local powder density (mg/mm^2).

4.2 Design of 2D Beamformer System

I designed and fabricated a Luneburg lens based beamformer. Beam scanning antenna arrays are critical components of many modern communication, navigation, and radar systems. In general, the position of the antenna's main beam is steered by controlling the amplitude and phase at each of the radiating elements. To accomplish this, a beamforming network is used. The Luneburg lens beamformer is a graded index device with attractive properties such as a wide bandwidth and a compact footprint [17, 37, 38]. In this example, I show how dry powder printing can be used to realize a mechanically robust passive Luneburg lens based beamformer.

The traditional Luneburg lens is a spherical device that transforms a point source excitation on its surface into a plane wave at the opposite side (Figure 4.14). The desired permittivity distribution to accomplish this is given by

$$\varepsilon_r(r) = 2 - \left(\frac{r}{R}\right)^2 \tag{4.10}$$

where R is the radius of the Luneburg lens and r is the radial distance from its center.

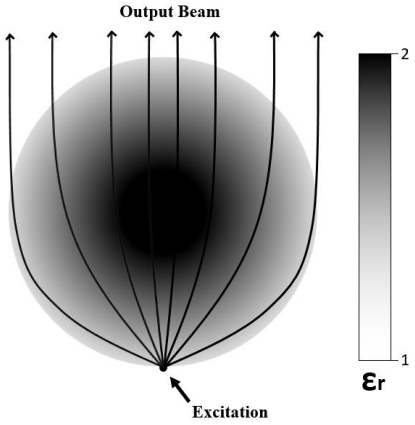

Figure 4.14: Overview of beamforming capabilities for a traditional Luneburg lens

In this example, I designed and fabricated a 2D Luneburg lens composed of a flat dielectric substrate sandwiched between two metallic plates in a parallel plate configuration (see Figures 4.15 and 4.18b). As in the case of the spherical Luneburg lens, the substrate's permittivity was spatially graded such that signals injected at one side of the lens (i.e., beam ports) are transformed into uniform waves with flat phase fronts on the opposite side (i.e., antenna ports). Exciting different beam ports produces varied resultant phase distributions at the antenna ports (see Figures 4.14 and 4.17). Thus, the particular beam port that is chosen determines the direction in which the beam is transmitted (i.e., beam steering). For my 2D device, the optimal permittivity distribution must be modified from the traditional Luneburg Equation (4.10). Thus, to determine the optimal permittivity distribution, I utilized the commercial software package HFSS, sold by ANSYS, and its integrated optimization tools.

My basic device configuration is illustrated in Figure 4.15. In this design, five beam ports, including SMA connectors, were uniformly positioned around a circular arc. On the opposite side (i.e., left hand side of Figure 4.15), 23 uniformly spaced antenna ports were integrated using tapered transmission lines. The taper was optimized to achieve a broadband impedance match over the 2 to 8 GHz band. Along the other sides of the device, I included 24 additional dummy ports with broadband 50 Ω terminations. These ports are needed to reduce unwanted side reflections. Within the circular region of the substrate, the permittivity was graded in the radial direction. To approximate a continuous permittivity grading, the circular region was divided into 25 equally spaced concentric rings (illustrated in Figure 4.15). Within each ring, the permittivity was assumed to be uniform with its value determined using HFSS simulations. More specifically, I performed an optimization over the 2 to 8 GHz band with the goal of maximizing the linearity of the phase distribution and the transmission efficiency at the antenna ports during excitation at each of the 5 beam ports. For these simulations, the permittivity was assumed to have a minimum value of ε_{min} =4.2 (i.e., base material) and a maximum value of ε_{max} =7.0 (i.e., printed with the highest packing density). The optimal permittivity distribution determined from HFSS simulations is shown in Figure 4.16. Here, the curve represents the desired permittivity within each of the 25 concentric rings.

Figure 4.17 presents full wave HFSS simulations for the 2D Luneburg lens when the permittivity distribution shown in Figure 4.16 is used. The subplots in this figure illustrate the predicted electric field intensity when the indicated beam ports are excited at 2.4 GHz. These simulations demonstrate how the excitation of different beam ports of the Luneburg lens steer the outgoing beam.

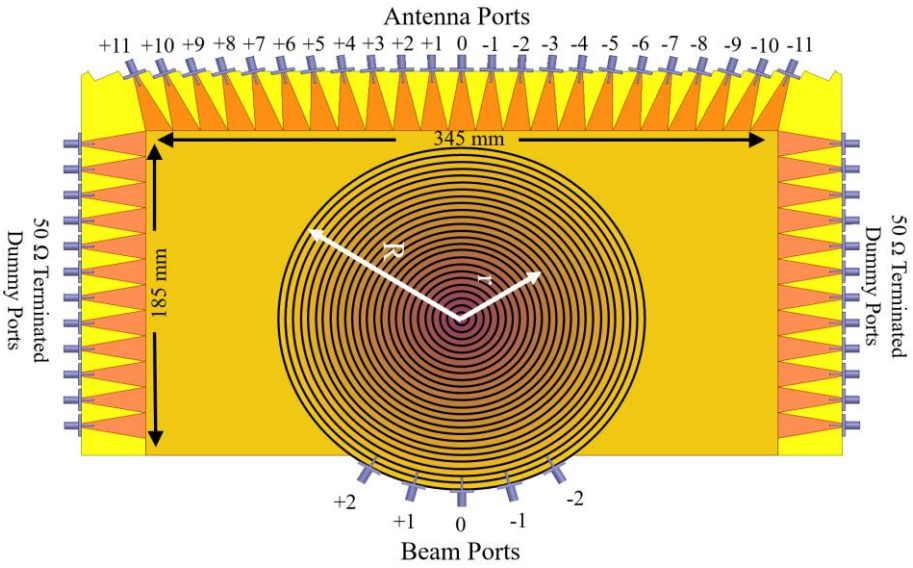

Figure 4.15: 2D Luneburg lens design configuration.

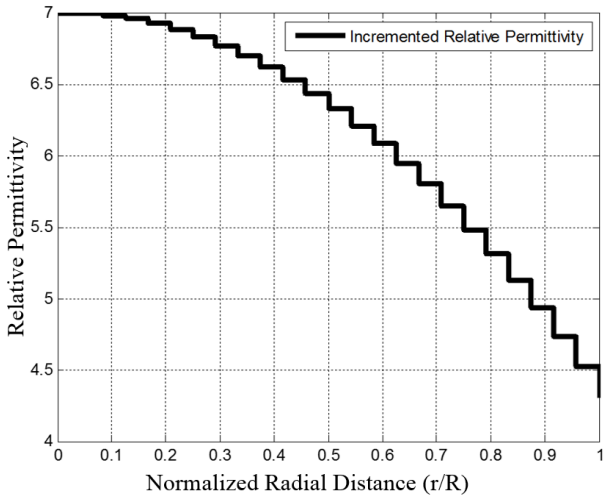

Figure 4.16: Desired permittivity distribution within circular region of 2D Luneburg lens determined using HFSS simulations. The curve represents the discrete desired permittivity within each of the 25 concentric rings illustrated in Figure 4.15.

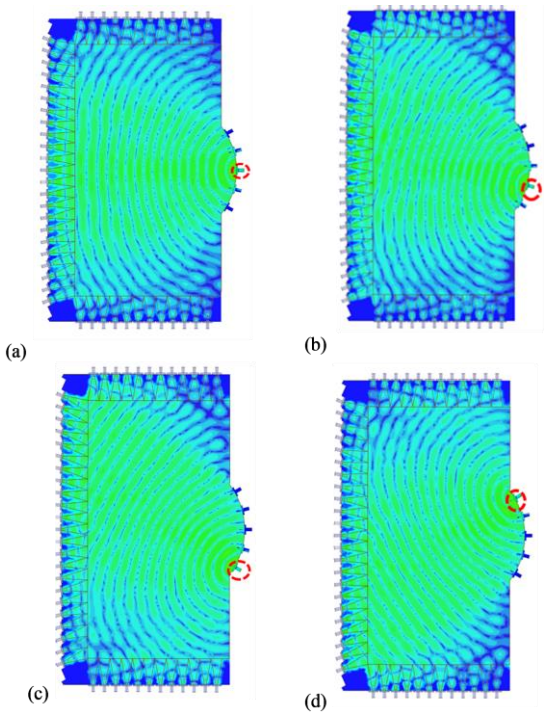

Figure 4.17: Electric field distributions computed using HFSS for the Luneburg lens beamforming network depicted in Figure 4.16. The dashed red circles in (a)-(d) indicate the location of the beam port that is excited. The graded permittivity distribution for these simulations is shown in Figure 4.16. The simulations were performed at 2.4 GHz.

4.3 Fabrication and Characterization

The device illustrated in Figure 4.15 was fabricated using dry powder printing with the substrate composed of 9 stacked layers of printed composite prepreg resulting in a total thickness of 2.02 mm. For each layer, the dry powder printer dispensed HiK ceramic powder on the uncured composite prepreg to create the local effective permittivity gradient given in Figure 4.16. This was achieved by printing concentric dotted rings in which the spacing between dots and rings was determined from the calibration curve in Figure 4.13. After stacking and post-curing, I acquired the mechanically robust substrate shown in Figure 4.18a.

The final part, shown in Figure 4.18b, was constructed by first adhering thin copper layers to both the top and bottom surfaces of the cured substrate. Then tapered microstrip transmission lines were chemically etched on the top surface at each of the antenna ports and side termination ports. Finally, standard SMA connectors were attached to all the input and output ports along with broadband 50Ω terminations at the side ports. Measurements from 1 GHz to 12 GHz were made using an Agilent PNA vector network analyzer. I characterized the performance of the device by measuring the transmission loss and phase delay of the transmitted signals at each of the antenna ports for input signals applied to each of the five beam ports (Figure 4.20). During these measurements, all input/output ports were terminated with 50 Ω loads except for the specific input and output ports being tested.

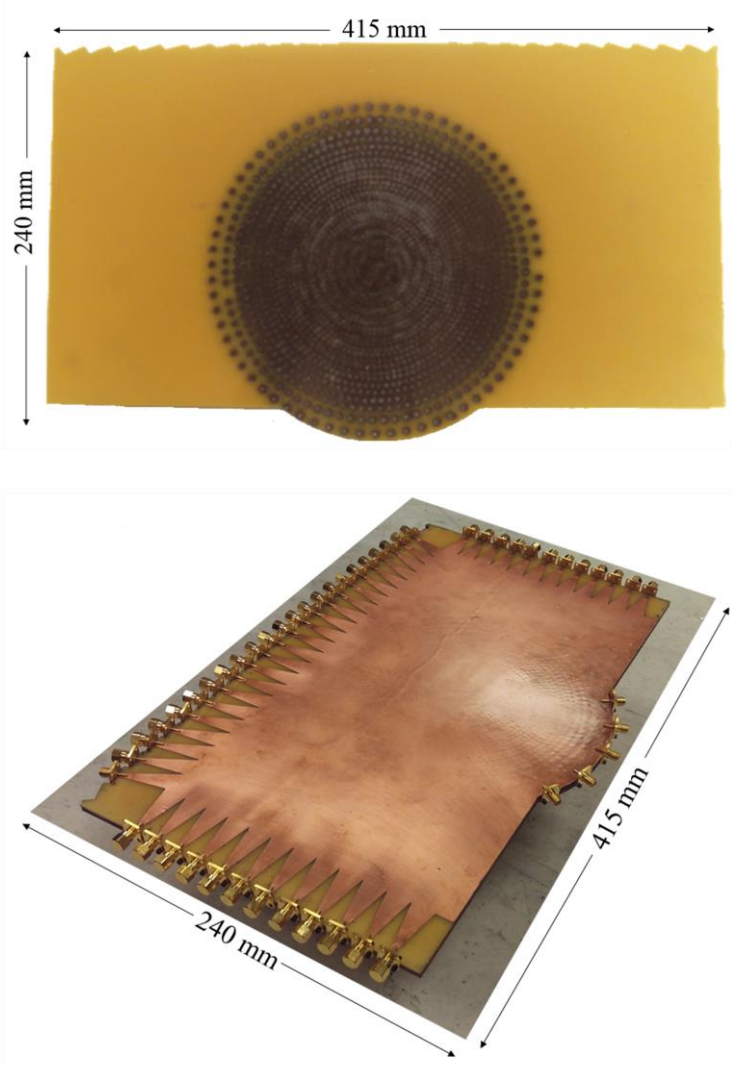

Figure 4.18: (a) Fabricated Luneburg lens substrate with spatially varying permittivity distribution produced using power printing, (b) Final fabricated part with etched copper top and bottom surfaces, SMA connectors and broad band 50 Ω loads attached to side ports to reduce unwanted side reflections.

I also measured the return loss at each of the beam ports to ensure that the input signals were well matched over the frequency band of interest (Figure 4.19).

Traditionally, a return loss below -10 dB suggests a sufficiently good impedance match, and this was achieved over the frequency band of 2.3-7.5 GHz.

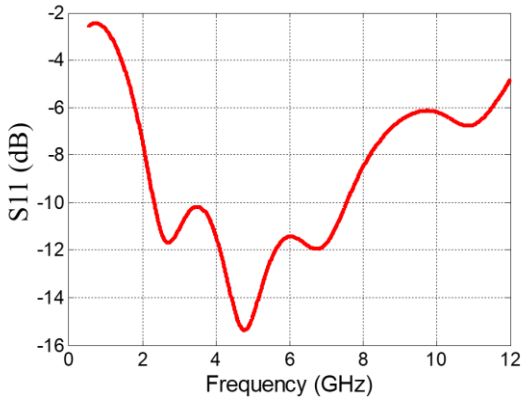

Figure 4.19: Return loss of center input port.

Shown in Figure 4.20 are the simulated verses measured phase delays and transmission losses at each of the 23 antenna ports. As shown in the plots, a linear phase variation between antenna ports occurs over a portion of the antenna ports. This is a result of the lensing effect that tends to concentrate the energy in a particular direction. The linear phase delay is most noticeable on the portion of the antenna ports in which the transmitted energy is the highest (see Figure 4.17). This effect will reduce the overall gain of the antenna pattern but will still produce beam steering as shown in Figure 4.21. As the selected beam port is varied, the slope of the linear phase delay varies accordingly. To show that the device will beam steer, I simulated the array

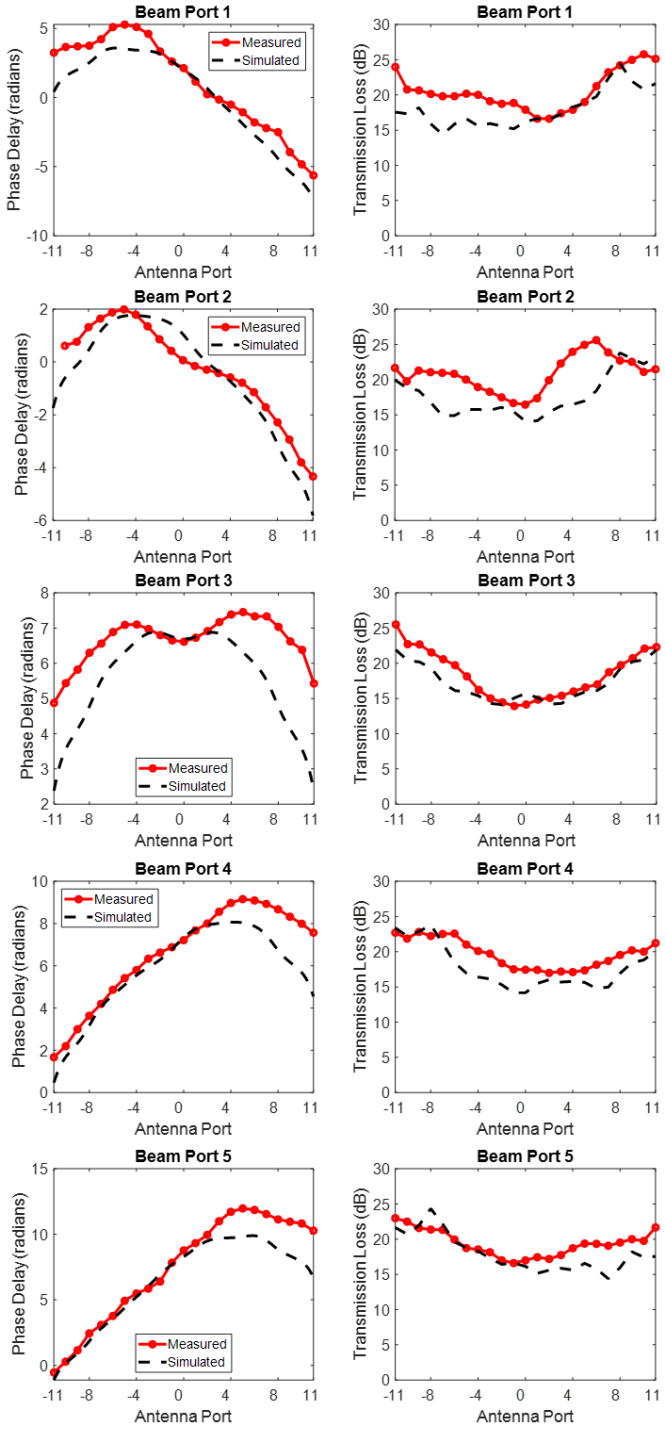

Figure 4.20: Measured phase delay and transmission loss at each of the antenna ports for a frequency of 2.4 GHz. The input port being excited varied: a) port #-2, b) port #-1, c) port #0, d) port #1, and e) port #2.

factor. In Figure 4.21, the array factor is plotted as a function of the far field azimuthal angle. In these simulations, I used the measured signals, shown in Figure 4.20, as the input sources to each of 23 identical antennas in the array. As shown in the figure as I switch beam ports, I obtain the expected steering of the radiation pattern for the array.

The discrepancies shown between the simulated and experimental results can be explained by two phenomena. First, the simulated model used perfect absorbing boundaries at the dummy and antenna ports. Whereas, in the fabricated system, reflections will exist due to imperfect matching at the port interfaces. These reflections can cause undesired constructive and destructive interference with incident waves. Second, the modeled dielectric distribution consists of 25 concentric rings that are optimized for beamforming. The fabricated system consists of powder dots that emulate the modeled dielectric distribution. Instead of using discrete rings, as shown in the model, I am using discrete powder dots to create an effective media gradient. This translates reasonably well but not perfectly. These two considerations are the driving factors for the small inconsistencies between the modeled and experimental results.

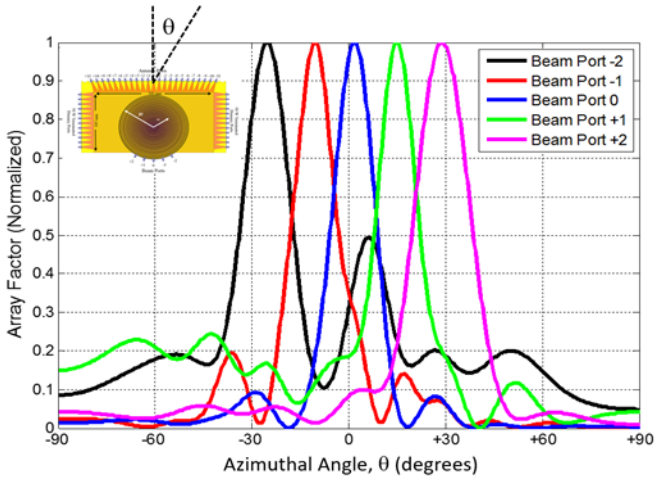

Figure 4.21: Simulated antenna array factor for the Luneburg lens beamformer for excitation at the five beam ports at 2.4 GHz. The measured antenna port signals, shown in Figure 4.20, were used as the input signals to calculate the array factors.

Chapter 5

ADDITIVELY MANUFACTURED LUNEBURG LENS BEAMFORMER

In this chapter, I will discuss the application of 3D Luneburg lenses for two unique beamforming systems: (1) ultra-wideband RF retroreflector and (2) ultra-wideband RF directional finder. Before discussing these applications, I will provide a description of how I fabricate Luneburg lenses using AM methods. Chapter 5.1 is a detailed overview of Larimore's work described in [42] and [48]. I will be leveraging this work to fabricate Luneburg lenses for the two applications described in Chapter 5.2 and Chapter 5.3.

5.1 Fabrication of Luneburg Lenses via Additive Manufacturing

One of the main challenges for fabricating a Luneburg lenses for antenna applications is the ability to fabricate the GRIN distribution through a practical and robust approach. Formerly, researches realized Luneburg lenses through two manufacturing methods: (1) casting and assembling various materials into spherical shells and (2) subwavelength texturing. Casting tends to be costly and slow. Subwavelength texturing compromises the mechanical robustness. To this end, a fused filament fabrication (FFF) fabrication technique will be used as an alternative manufacturing method to casting/assembling and subwavelength texturing.

In Liang et al [37], the investigators showed the ability to fabricate a Luneburg lens through additive manufacturing. This was achieved by 3D printing a GRIN lens through polymer jetting. This approached leveraged a UV-curable polymer. The

polymer is deposited and cured layer-by-layer. For each layer, the process is repeated until the 3D pattern is complete. In order to create a permittivity that varied spatially, Liant et al. used the single unit cell configuration illustrated in Figure 5.1. The local effective dielectric constant is realized by ratio of the length of the center cube to the spacing between each unit cell. This assumption is permitted when the single unit cell size is smaller than the effective wavelength ($\Lambda << \lambda$).

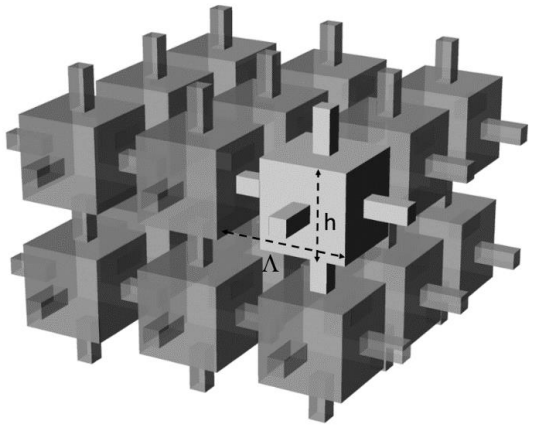

Figure 5.1: Geometry used in [37] for creating a spatially-varying permittivity distribution using UV-curable polymers

Through the manufacturing approach described in [37], the investigators demonstrated an operational Luneburg lens. The lens had gain figures above 20 dBi in the X-band. This functional Luneburg lens demonstrates an advancement in additive manufacturing and the design of graded refractive index structures. However, there are drawbacks and limitations with this polymer jetting AM approach. Firstly, the polymer jetting method does not create self-support geometries. As a result, it requires support materials to be printed between unit cells. The supporting materials significantly raises

print time and is hard to vacate the support structures from these complex geometries after fabrication. Secondly, this process utilizes UV-curable polymers. UV-curable polymers have significantly higher loss-tangents when compared to non-UV curable polymers [38]. This is more pronounced at frequencies exceeding 18 GHz. Thirdly, UV-curable polymers structurally degrade over an extended period of time. Lastly, polymer jetting systems and the materials used are quite expensive. To illustrate this, UV-curable polymers used in this system cost over $1,000 per kilogram.

At the University of Delaware, investigators have created a new additive manufacturing approach for creating the Luneburg lens. This technique uses a fused filament fabrication (FFF) deposition method. FFF alleviates some of the disadvantages of the polymer jetting technique. Firstly, FFF is a more common technique. There are several commercially FFF systems available for purchase. Secondly, FFF is more cost-effective in comparison. FFF systems can be bought for a price less than $1,000. The printing materials cost less than $100 per kilogram. Thirdly, FFF is not confined to one thermoplastic materials. These thermoplastic materials include polycarbonate, polypropylene, polyethylene, acrylonitrile butadiene styrene, and polylactic acid. These materials have low loss-tangents and nondispersive characteristics from DC to W-band. Lastly, by leveraging the space-filling curve technique described in the following section, it is possible to realize mechanically strong Luneburg lenses.

5.1.1 Fused Filament Fabrication

To fabricate Luneburg lenses, I employed the FFF 3D printing method illustrated in Figure 5.2. In FFF, a thermoplastic feedstock is extruded from a heated nozzle. The extruded filament is then stacked layer-upon-layer. When the extruded

filament is deposited onto a previously deposited layer, the hot extrudate partially melts the previous layer creating a bond and then rapidly cools to lock in the desired shape. The smallest printable feature size achievable using FFF is a function of the diameter of the heated nozzle and the precision of the mechanical stages.

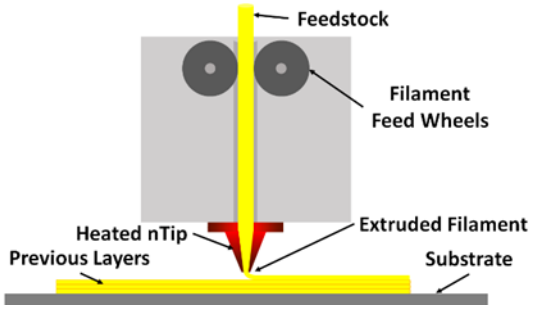

Figure 5.2: Illustration of FFF printing process

In developing an approach for realizing GRIN structures using FFF, several practical considerations should be satisfied. First, it is advantageous to avoid the use of sacrificial support material. These materials increase both the time and cost of fabrication, and are often difficult to remove entirely from the final part. Without the use of support material non-self-supporting geometries, such as the one shown in Figure 5.6, are not possible. Second, it is desirable to minimize the number of starts and stops needed during the print process. Too many starts and stops can adversely affect the mechanical rigidity of the part and often leave excess strands of polymer that alter the local dielectric properties in an unpredictable manner. In fact, if possible, it is desirable to print the entire 3D structure using one continuous curve. Third, I want to use a geometry that will produce a mechanically robust final part. To this end, I employed the space-filling curve approach described in the next section.

5.1.2 Space-Filling Curves for Creating Graded Permittivities

Late 19th century, Peano and Hilbert introduced the fundamental characteristics of the space-filling curve. The characteristics of the space-filling curves permit the ability to entirely occupy higher dimensional space and be continuous [40-41]. Since the inception of space-filling curves, different space-filling curves have been explored and applied for various applications. These applications include antenna design and image processing. In this section, a technique for using space-filling curves to create 3D graded refractive index structures [42] will be explained in detail. The Peano-type is selected for its geometry shown in Regazzoni [43] and Figure 5.3(a). The curves illustrated in Figure 5.3(a) consists of an individual unit cell. The number of turns (N) determines the localized volume fraction of material found within a single unit cell. The localized volume fraction of materials defines the effective permittivity. The individual unit cells are configured so that the starting and ending points are found at the same corner. This allows each layer of the print to be created by one continuous curve. This effect is illustrated in Figure 5.3(b). This feature is crucial while fabricating graded refractive index structures.

5.1.3 Modeling the Anisotropic Permittivity of the Unit Cell

The ability to design a 3D graded refractive index system involves the understanding how the pattern of the unit cell affects the effective permittivity. One disadvantage of the space-filling technique: the electromagnetic field oriented in the z-axis will have a differing volume of printed material than that of the fields in the xy-axes. As a result, an anisotropic effect will be inherent in this printing method.

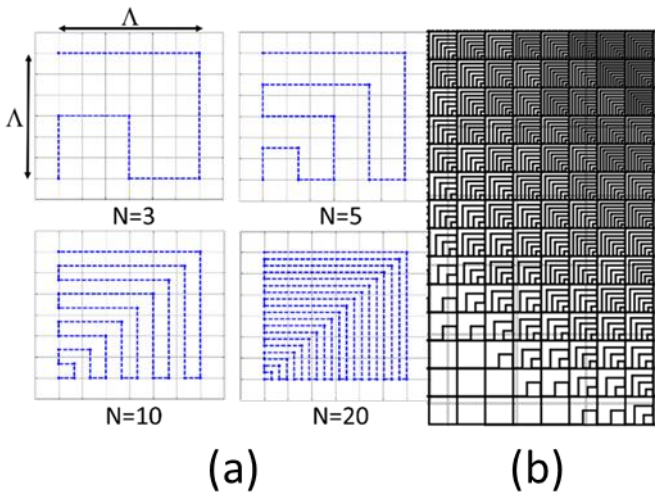

Figure 5.3: (a) Space-filling configuration utilized to create spatially-varying relative permittivites. (b) Each unit cell can be aligned and oriented into rows and columns. Also, they can graded using one continuous material curve.

Thus, the anisotropic permittivity of the space-filling curve geometries are modeled using effective media theory (EMT). EMT is an accurate approach as long as the unit cells are smaller than the material wavelength ($\Lambda << \lambda$). For simple geometries, analytical mixture formulas have been derived to estimate the effective permittivity; however, for more complex geometries such as the space filling curves, a computational approach was required. Figure 5.4 shows a detailed illustration of an FDM-printed unit cell where the cross-sectional area of a printed filament is given by

$$A_{cross} = h(W-h) + \pi\left(\frac{h}{2}\right)^2, \tag{5.1}$$

W indicates the diameter of the extrusion nozzle. h indicates the thickness of the printed layer. Volume fraction (VF) is equal to the Equation 5.2.

$$VF = \frac{A_{cross} \cdot L_{tot}}{\Lambda^2 \cdot h}, \tag{5.2}$$

Λ^2 is the area of a unit cell. L_{tot} indicates the total length of the printed material in a single unit cell. The formula to solve for L_{tot} is shown in Equation 5.3.

$$L_{tot} = (N+1)\Lambda \tag{5.3}$$

Substituting (5.1) and (5.3) into (5.2) gives an expression for the volume fraction of printed material within a unit cell as a function of the filament shape and the space filling parameters:

$$VF = \frac{\left(W - \left(1 - \frac{\pi}{4}\right)h\right) \cdot (N+1)}{\Lambda} \tag{5.4}$$

The modeled is validated through the fabrication of samples consisting of different volume fractions. The measured values are indicated by the asterisks shown in Figure 5.5. The modeled and measured parts suggest excellent agreement [42].

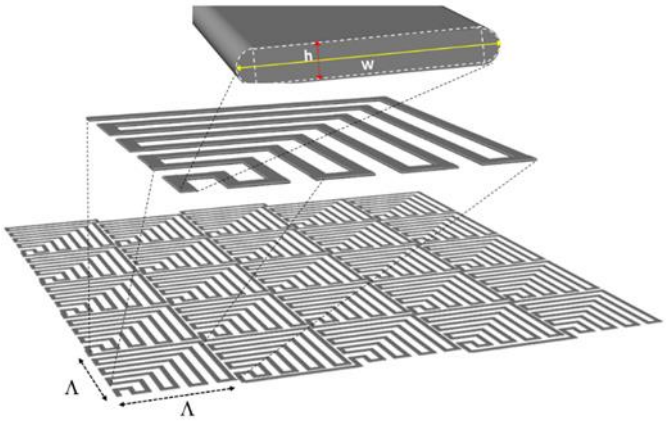

Figure 5.4: Detailed illustration of cross-sectional shape of printed space-filling curves via FFF. The volume fraction of printed material in each unit cell is a function of the order of the space-filling curve and the print geometry of the polymer filament.

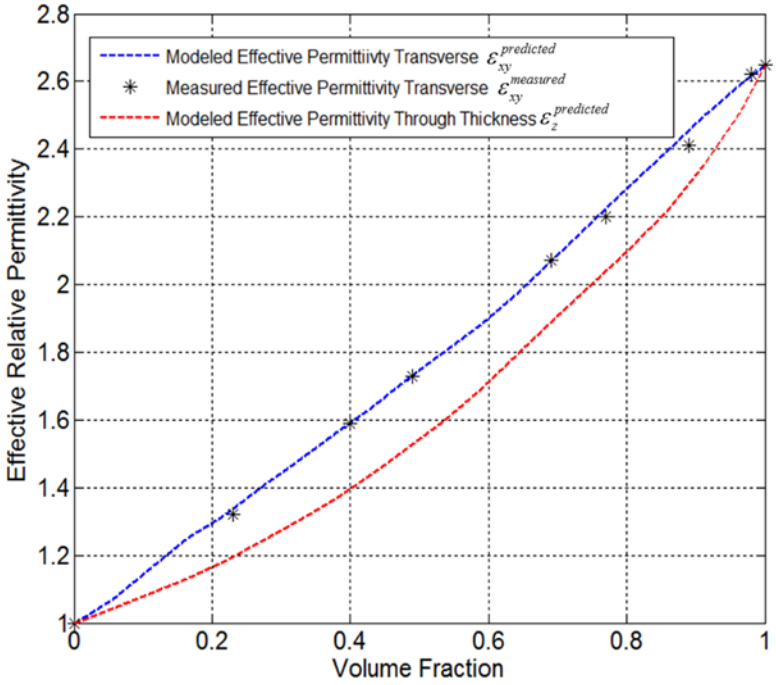

Figure 5.5: The predicted and measured relative permittivity of the space-filling curve geometry as a function of volume fraction.

5.1.4 Effect of a Low-Permittivity Base on Luneburg Lens Performance

It is more practical to have an excitation region that is planar. For that reason, a low dielectric constant scaffolding base will be used. This is illustrated in Figure 5.6. The scaffolding serves two purposes: provides a planar surface to attach excitations and allows for a single print without needing a sacrificial supporting material. The electromagnetic effect of the support structure is simulated in High Frequency Structure Simulator (HFSS). In HFSS, two different models were compared: one with the supporting material and one without the supporting material. For the model with the base structure, an open-ended waveguide at various positions was used to excite the Luneburg lens. For the waveguide excitation, a waveport was used to excite the fundamental mode of the waveguide. These simulations focused on the K_a frequency

band gain responses of a 40 mm diameter Luneburg lens. Therefore, a WR28 waveguide was used. The permittivity distribution of the lens follows Equation 3.1. The base structure had an effective permittivity of $\varepsilon_{base} = 1.2$. To determine the effects of the dielectric base, simulations were done on the same lens without a dielectric base. For the simulations without the dielectric base, an open-ended waveguide excited the lens by conformally places the waveguide to the surface of the spherical lens. This is illustrated in Figure 5.6(b).

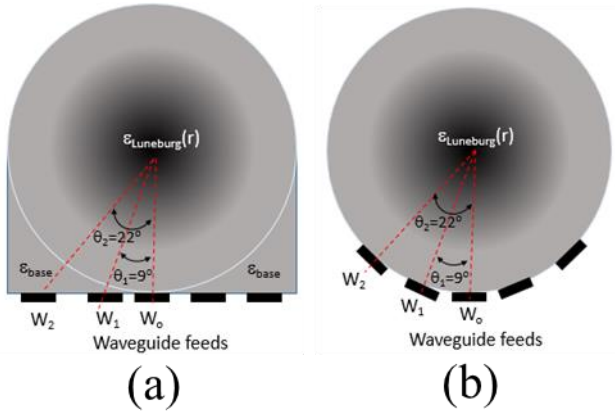

Figure 5.6: Luneburg lens models used to predict the effect of adding a low-permittivity base onto a spherical Luneburg lens. W_0, W_1, and W_2 denote the locations used to predict performance as the open-ended waveguide feed is moved from the center location.

Figure 5.7 shows the simulated results. The simulations show the antenna gain as a function of azimuth angle at a particular frequency. For the simulations shown in Figure 5.7, the results are for 30 GHz. The open-ended waveguide was positioned at the following locations: W_0, W_1, and W_2. This is illustrated in Figure 5.6(a) and Figure 5.6(b). At feed location W_0, the antenna gain, in the far-field, was reduced by a small

amount due to the scaffolding base. A reduction of 0.2 dB was observed. As the waveguide excitation was moved off center, shown by position W_1 and W_2, the gain performance reduction became greater. At waveguide position W_2, the peak gain showed a 1.5 dB reduction in performance. It is also worth mentioning that the side-lobes became much larger for the model with the dielectric base. This phenomenon can be explained by the fact that the waveguide is effectively further away from the surface of the Luneburg lens. The focal plane is directly at the surface of the Luneburg lens. If a source is further away from the focal plane, the beamforming effect is not optimal. In conclusion, the practicality of the planar scaffolding overshadow the compromised antenna gain performance.

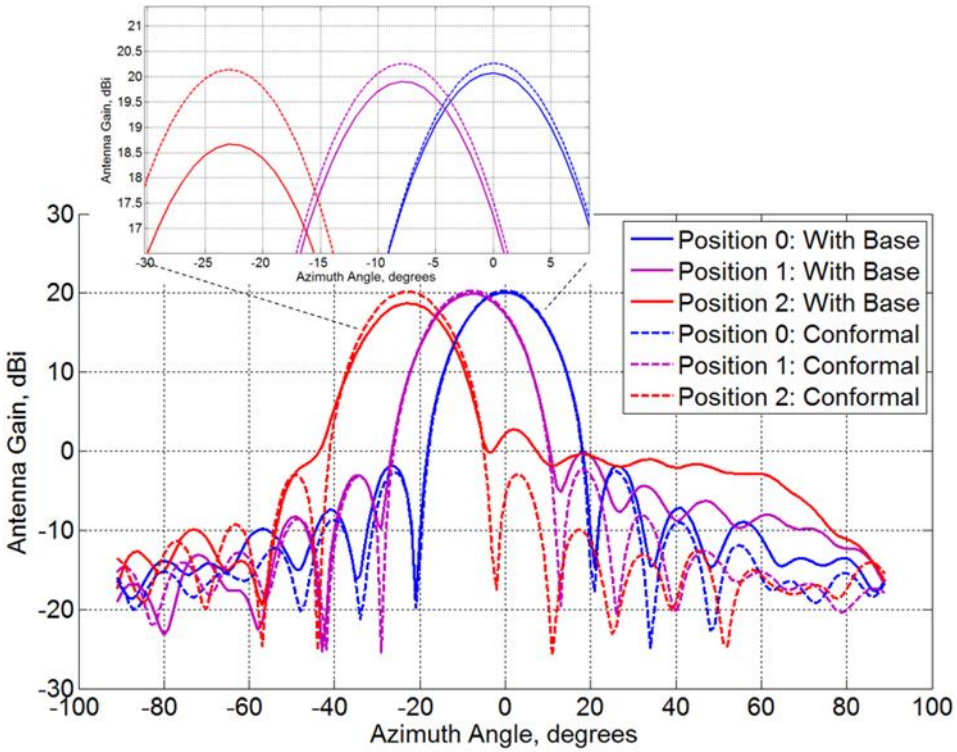

Figure 5.7: Simulated antenna gain of the K_a-band Luneburg lens antennas illustrated in Figures 5.6(a) and 5.6(b). The simulations were conducted at 30 GHz with the excitation source placed at locations W_0, W_1, and W_2 shown in Figure 5.6. The results present the effect of adding a low permittivity base structure on the performance of the Luneburg lens.

5.1.4.1 Effect of Anisotropic Effective Permittivity on Luneburg Lens Performance

The fabrication approach described earlier has anisotropic permittivity. An HFSS simulation was done to understand how this anisotropy affects the Luneburg lens' gain performance. Two separate models were used: one model with an isotropic permittivity tensor and one model with an anisotropic permittivity tensor shown in Figure 5.5. In these two models, the dielectric base was used (Figure 5.6(a)). The simulations were done at 30 GHz. The lens was excited with an open-ended waveguide at positions W_0 and W_2. The far-field gain results are a function of azimuth

angle. These results are illustrated in Figure 5.8. Figure 5.8 suggests that the anisotropic permittivity effect is insignificant. This remains true even at the most off-center position W_2. At W_2, the peak gain reduction is less than 0.1 dB.

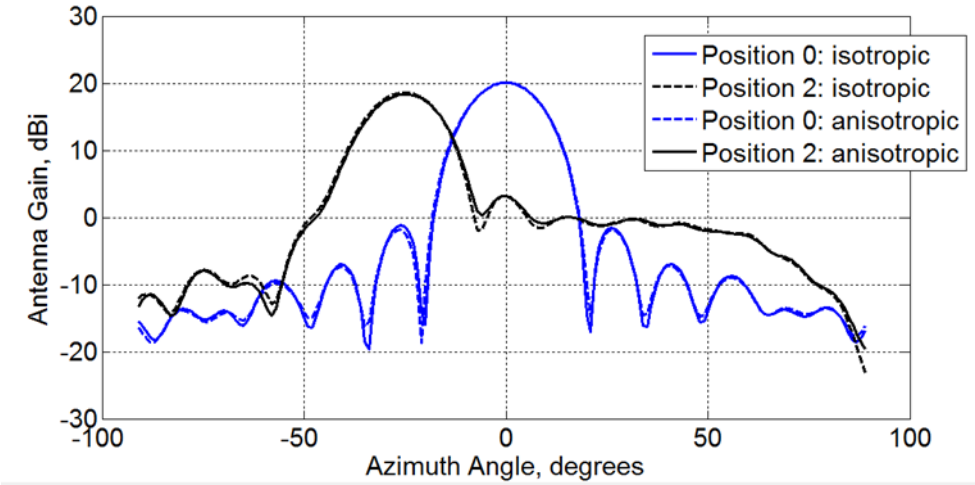

Figure 5.8: 30 GHz simulation of antenna gain. Antenna excitation locations include W_0 and W_2 (shown in Figure 5.9(a)). The traces in this figure illustrate the gain for the perfectly isotropic lens and the anisotropic permittivity shown by Figure 5.5.

5.1.5 Luneburg Lens Design

To design 3D Luneburg lenses using space-filling curves, the following process was employed. The first step is to slice the desired three-dimensional permittivity distribution, given in Equation (3.1), into a series of uniform thickness layers. The slice thickness (i.e., print-layer thickness) depends heavily on the chosen print parameters but is typically required to be a value less than half the diameter of the print nozzle. The continuous permittivity distribution of each layer is then divided into an array of unit cells as shown in Figure 5.9(b). The size of each unit cell should

be smaller than the shortest wavelength of operation. The desired volume fraction for each unit cell is then calculated using the EMT described previously and illustrated in Figures 5.3 and 5.4. Using these results, a space filling curve with the correct number of turns, N, is generated for each unit cell as shown in Figure 5.9(c). This process is then repeated for each slice of the desired geometry. All of the individual layers are then stacked vertically (Figure 5.9(d)) to realize the final 3D Luneburg lens. Once the continuous space filling curves are calculated, a custom MATLAB code is used to generate the tool path needed to realize the printed part. It should be noted that the space-filling curve intersects the border of each unit cell, thus allowing high fill fraction layers to be printed onto low fill fraction layers without compromising structural integrity.

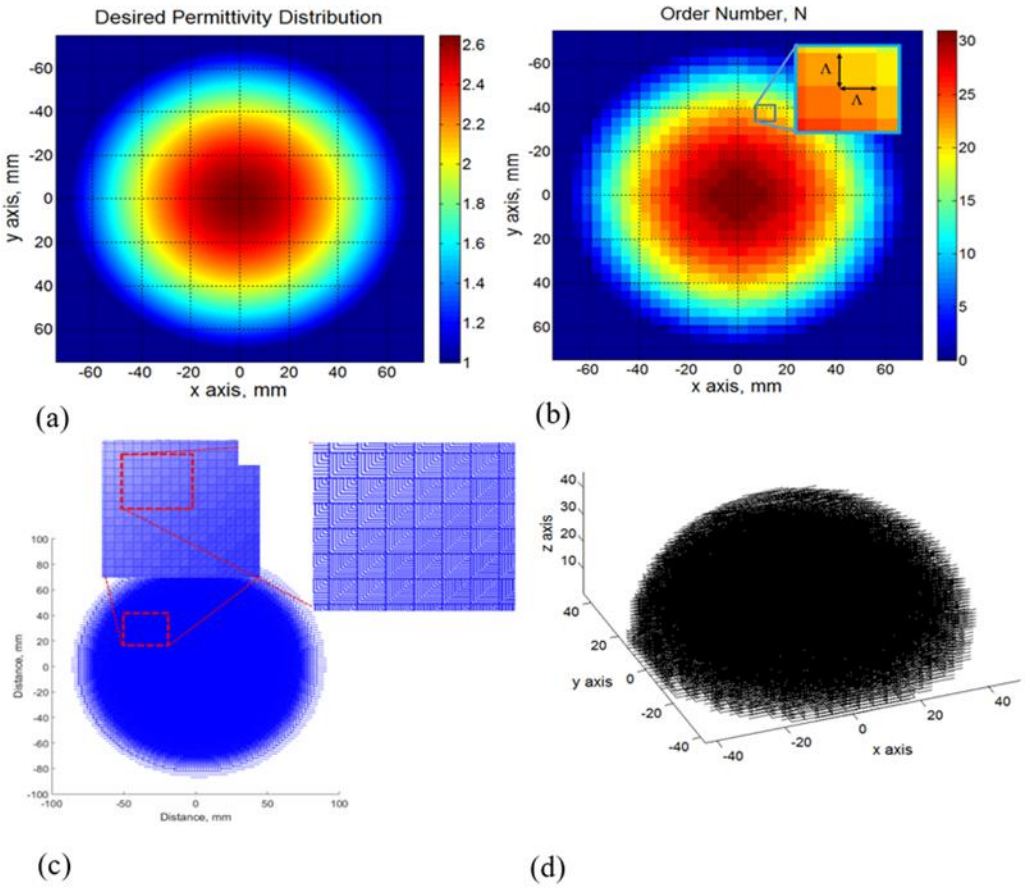

Figure 5.9: Timeline of fabricating a 3D GRIN Luneburg lens. (a) Desired permittivity distribution. (b) The permittivity distribution is separated into individual voxels that follow the desired permittivity distribution. (c) Using the space-filling curve technique, each voxel is assigned a space-filling pattern to correspond to an effective permittivity. These patterns are stacked in the z-direction. (d) The voxels are populated and the part is fabricated layer-by-layer.

5.1.6 Fabrication

For fabrication, an nScrypt™ 3Dn-300 system, shown in Figure 5.10, was used. The nScrypt 3Dn-300 is a quad deposition system. Each head can be outfitted with various AM attachments: paste extrusion, FDM, pick-and-place, and milling. For fabricating the Luneburg lenses, only the FDM deposition system is used. The nScrypt

3Dn-300 is also outfitted with a 3D laser scanning system, 300mm x 300mm heated build plate, and fiducial alignment camera. Another feature of the nScrypt is its ability to print lines as thin as 20 µm. Also, the stages have position accuracy as low as 1 µm. The system is illustrated in Figure 5.10.

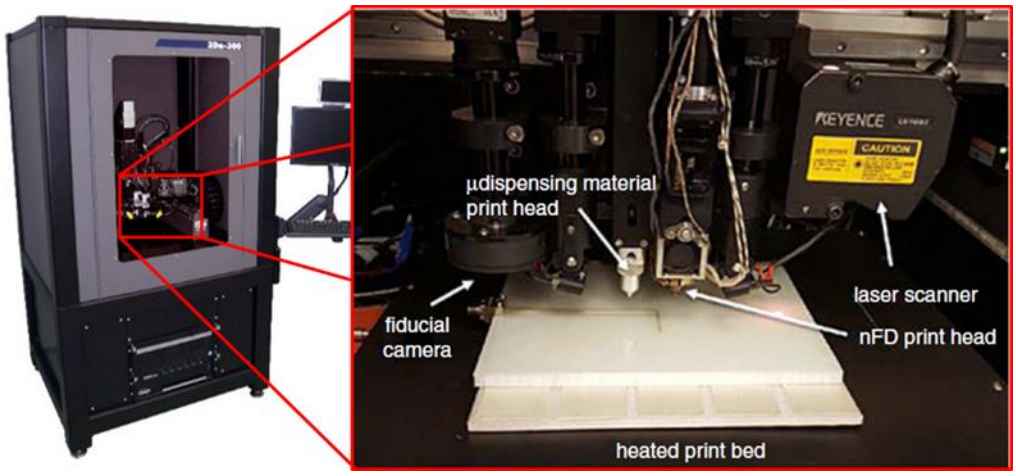

Figure 5.10: nScrypt 3Dn-300 system used for FFF fabrication of Luneburg lenses.

The thermoplastic chosen for fabrication of the Luneburg lenses was a polycarbonate obtained from matterhackers.com. This material demonstrates excellent EM properties, as well as a wide range of desirable mechanical properties. EM characterization of the polycarbonate material was done over a wide band of frequencies (8 - 110 GHz) using a free-space focused beam method [44]. Those measurements determined that the material was relatively non-dispersive over that frequency range with a dielectric constant of $\varepsilon_r = 2.68$ and a loss tangent of $\tan \delta = 0.002$. In comparison, most UV-curable polymers used in additive manufacturing have loss tangents of $\tan \delta > 0.02$ [39].

5.2 Application #1: Ultra-Wideband RF Retroreflectors

5.2.1 Introduction

The usage of reflective devices for purposes of radar cross section (RCS) augmentation and calibration is ubiquitous within the radar test and measurement community, with civilian uses for radar navigation and avoidance being proposed shortly after World War II [45]. Early works in this area recognized the merits of utilizing the high-gain dielectric structure of Luneburg lenses to achieve a wide acceptance angle for reflection [46], however; early lenses were difficult to manufacture in three dimensions due to a lack of materials with a continuously variable index of refraction [47]. For these reasons, spherical Luneburg lens devices are often manufactured using a stepped-index construction.

Recent advances in additive manufacturing (i.e. AM or 3D printing) have allowed for graded-index structures of nearly arbitrary shape and permittivity distribution to be fabricated. The required refractive index at any small region within the volume is related to the percentage, or fill factor, of printed material verses air voids. To vary the fill factor, I employed the "space-filling curve" [42] technique described in Chapter 5.1. By using the spacefilling curve technique along with a simple metallic surface coating, I was able to create a lens based retro-reflector that can be used to augment the RCS of an item across a nearly 140-degree cone angle.

5.2.2 Reflector Design, Fabrication, and RCS Performance

The reflector's dielectric lens permittivity distribution was realized using the space-filling curves concept described in [42] and 3D printed on an nScrypt 3Dn-300 system.

5.2.2.1 Design

The retroreflector design was inspired by the beamforming capability of the Luneburg lens.

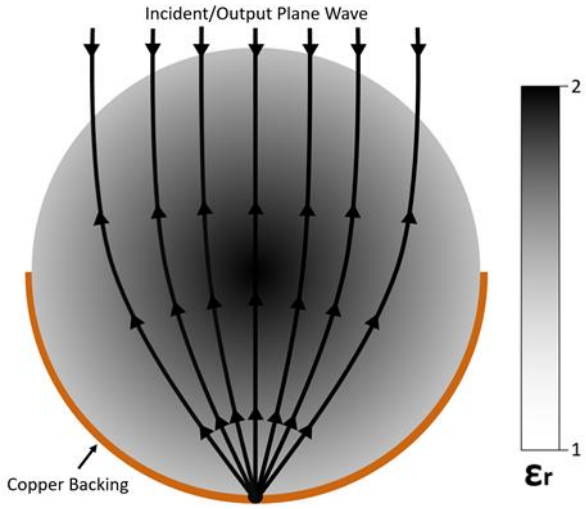

Figure 5.11: Propagation of power through Luneburg lens retroreflector

The main feature of the Luneburg lens is that every point on the surface acts as a focal point for a plane wave incident from the opposite surface of the lens. This relationship is reciprocating. The reciprocating relationship is leveraged to achieve the retroreflective effect. For the retroreflector, I am exciting the lens with a plane wave. The plane wave propagates through the lens where it is focused onto a hemispherical copper layer that has been applied to reflect power back through the lens. The returning reflected power exits the front side of the lens as a plane wave traveling along the same optical path as the incident wave but in the opposite direction. This phenomenon yields a high radar cross-section for a wide range of incident angles. The configuration of lens and copper backing is illustrated in Figure 5.11.

5.2.2.2 Fabrication

The fabrication of the Luneburg lens leverages the spacefilling curve method shown in Chapter 5.1. Luneburg lens design, for the retroreflector, is a 120 mm diameter lens with a supporting base. The lens is then divided into voxels with a period of 4 mm and each voxel has the appropriate volume fraction of polycarbonate to achieve the effective dielectric constant that follows the Luneburg equation. This process is illustrated in Figure 5.12. The fabricated lens is capable of operating over frequencies that range from 8-30 GHz.

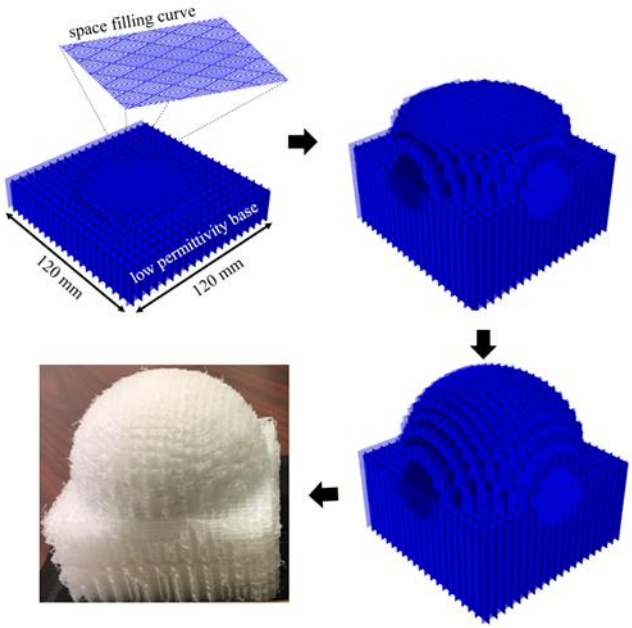

Figure 5.12: Illustration of the FDM layer-by-layer printing process of the Luneburg lens retroreflector using space filling curves.

Upon completion of the additive manufacturing process, a set of copper tape strips were overlapped onto the rear hemisphere of the lens to create a simple end-cap reflecting surface. The device and end-cap structure can be seen in Figure 5.13.

Figure 5.13: View of the copper tape placed over the spherical end cap of the reflector.

5.2.2.3 RCS Modeling Methodology

High-Frequency Structure Simulator (HFSS) was used for electromagnetic modeling and simulations. HFSS predicted a full 360 degree RCS measurements for the fabricated lens at the various frequency bands. The simulated model consists of the fabricated Luneburg lens, a metal backing, and the low permittivity dielectric base. In the model, the Luneburg lens was approximated by five concentric spheres with varying relative permittivities that correlate with the Luneburg dielectric distribution. The metal backing is a perfect electric conductor (PEC). The excitation for the RCS

measurements was a plane wave at various incident angles. Figure 5.14 illustrates the configuration of the components.

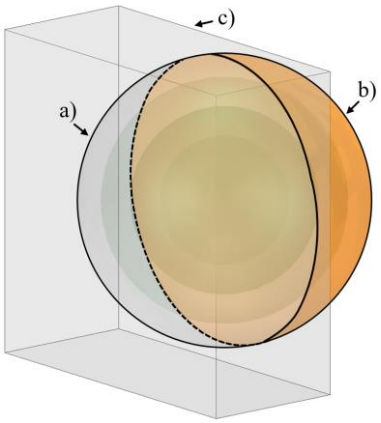

Figure 5.14: HFSS model of retroreflecting system consisting of a (a) Luneburg lens, (b) metal reflector, and (c) low permittivity dielectric base

5.2.2.4 RCS Measurement Methodology

To measure the RCS of the retro-reflector, a series of data collections were undertaken within an anechoic chamber. The device under test (DUT) was placed within the quiet zone of the chamber on a rotating pedestal of polystyrene foam having a dielectric constant of ~2.5 relative to air. The measurement setup included a commercially available Agilent Vector Network Analyzer (VNA) along with a set of wide-band horns. The horns were chosen to cover the full bandwidth of the VNA (i.e. 700 MHz – 44 GHz) with a break-point at 18 GHz between the two sets of horns.

The chamber setup can be seen in Figure 5.15, while the VNA configuration is shown in Figure 5.16. The VNA measurements were taken in 1.0 degree increments using a set of automation scripts. The results were then calibrated using the subtraction method as described in [49], where a set of background data were collected with no

DUT in the chamber in order to coherently subtract out the background. Finally, a calibrated corner reflector was measured in place of the DUT to provide a calibrated RCS response for the processed results. The processed results are shown in the following section.

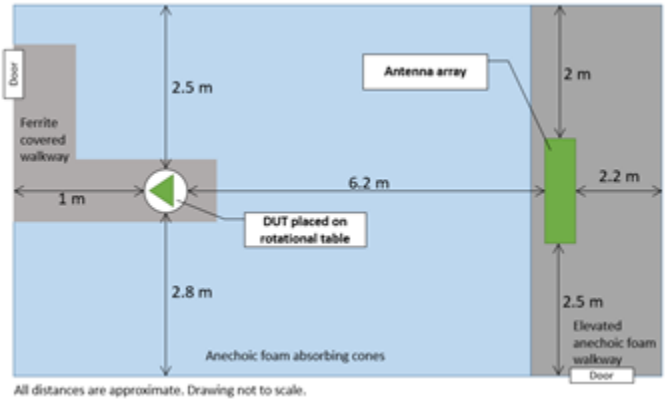

Figure 5.15: RCS measurement setup

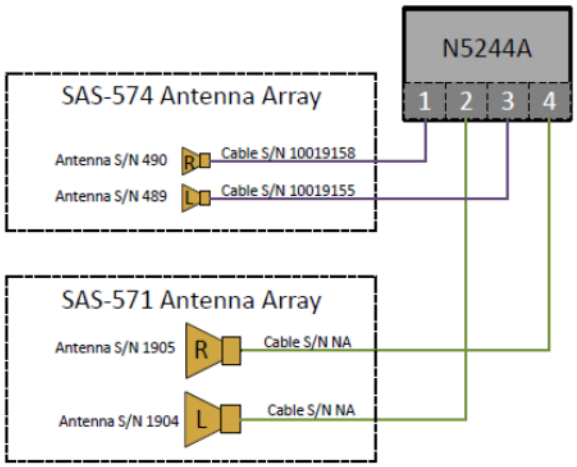

Figure 5.16: Vector Network Analyzer and Antenna Array Configuration

5.2.3 Results

The simulated and measured results for X, Ku, and K bands (10 GHz, 16.7 GHz, and 22.5 GHz centers respectively) are shown in Figures 5.17-5.19. The additional lobe structure of the measured data within the back lobe is due to the tape "slats" that make up the end-cap. These can likely be eliminated via application of a smooth, one-piece-construction end cap. The results for Ku-band in Figure 5.18 are the most consistent between the measured and simulated RCS plots. This result is intuitively satisfying since the unit cell size of the space-filling curves used in the generation of the test unit is most appropriate for these frequencies.

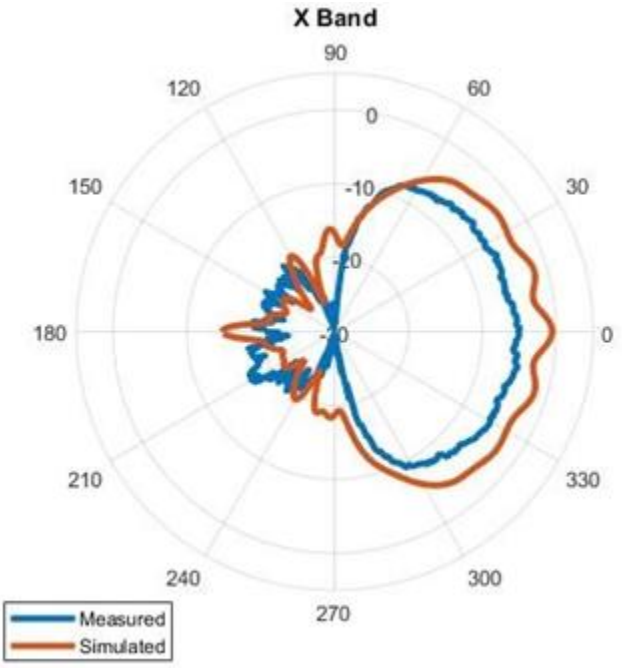

Figure 5.17: Measured (blue) and simulated (orange) radar cross section for the additively manufactured retro-reflector at 10 GHz

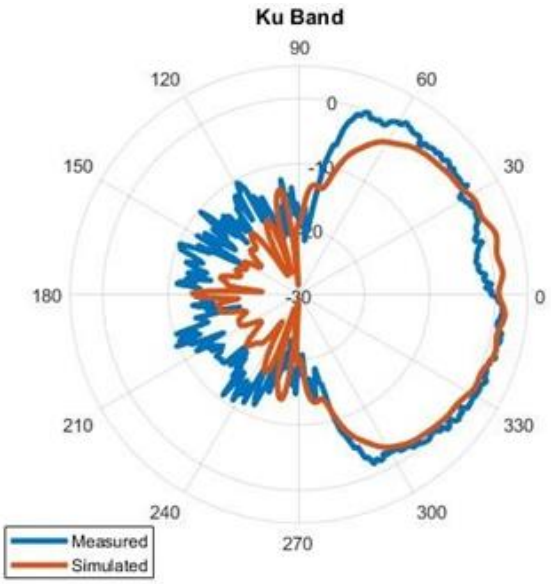

Figure 5.18: Measured (blue) and simulated (orange) radar cross section for the additively manufactured retro-reflector at 16.7 GHz

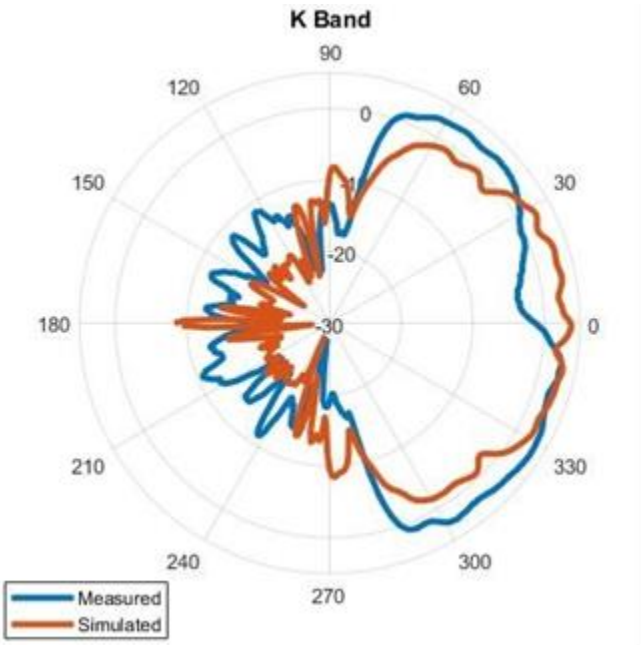

Figure 5.19: Measured (blue) and simulated (orange) radar cross section for the additively manufactured retro-reflector at 22.5 GHz

5.2.4 Conclusions

The results found in this work demonstrated that is possible to leverage the Luneburg GRIN lens to create a high radar cross section system with ±70 degree elevation and azimuth acceptance angles. The measured and simulated results display good agreement. The reasons for minor discrepancies can be explained by the following reasons: the FDM voxel size is optimized for Ku-band and the copper backing is not perfectly conformal. This work revealed additively manufactured Luneburg lenses are suitable for RCS augmentation and calibration systems.

5.3 Application #2: Ultra-Wideband RF Directional Finding

5.3.1 Introduction

Simultaneous localization and tracking of multiple radio frequency (RF) emitters is critical for a host of civilian and military applications, such as mobile communication networks, search and rescue operations, and situational battlefield awareness. For these applications, conventional approaches are often too costly or difficult to deploy. This is particularly true when localizing multiple emitters that may cover a large frequency band and a wide range of source locations. I describe here an approach based on the integration of a passive graded index (GRIN) beamforming lens with a 2D planar array of small receive antennas. My device, similar to a conventional imaging system, focuses radiation incident from a particular direction onto a corresponding detector placed along the back side, or focal plane, of the lens. One novelty of my implementation is the design and fabrication of the 3D GRIN lens. Specifically, I have leveraged advancements in additive manufacturing (AM) to develop a methodology for fabricating GRIN lenses using low cost fused deposition modeling (FDM) 3D printers and polymer filaments [42, 48]. This lens, when

combined with a 2D array of receive antennas, power detector chips, and associated electronics results in a system capable of determining the direction and intensity of multiple RF emitters over a large band of frequencies (e.g., K to Ka bands) and a wide instantaneous field of view.

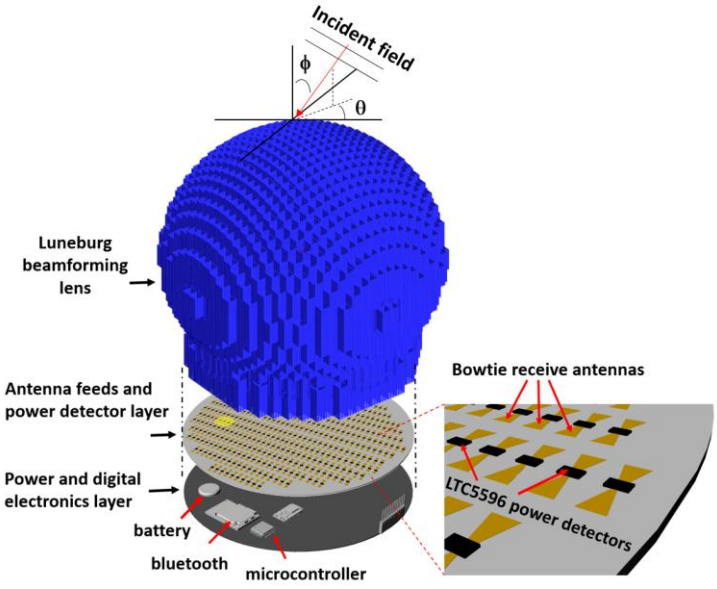

Figure 5.20: My system for detection of multiple RF emitters consists of a custom designed and fabricated 3D GRIN lens with planar focal plane, a 2D array of small receive antennas and LTC5596 power detector chips, battery power, associated read out electronics and wireless data transmission circuitry.

5.3.2 Experimental Details

My system, illustrated in Figure 5.20, integrates three primary subsystems to detect the direction and intensity of incident radiation emanating from one or multiple sources. Namely, (1) an additively manufactured graded index Luneburg lens, (2) an array of broadband bowtie receive antennas and integrated power detection chips

(LTC5596), and (3) an electronics layer that includes battery power, digital controller, and Bluetooth for wireless data transmission.

5.3.2.1 Graded Index Lens

My system design was inspired by the wideband passive beamforming capabilities of the Luneburg lens. There are three principal features of the Luneburg lens that make it an attractive solution for RF localization. First, any point on the surface of the lens is a focal point for an incident plane wave on the opposing side. Second, the lens is ultra-broadband with no frequency restrictions on the beamforming effect as long as the diameter of the lens is larger than the illuminating wavelength in free space ($d>>\lambda_o$). Third, the lens allows for multiple beams to be detected simultaneously. It should be noted that these features are difficult to achieve with active phased array technology. To fabricate the Luneburg lens for this system, the spacefilling curve technique, presented in Chapter 5.1, will be used. After fabrication, I characterized the radiation pattern of the Luneburg lens using the system shown in Figure 5.21(b). This measurement system utilizes a standard gain horn as a reference port, and a waveguide (WG) abutted against the backside of the lens as the feed. Measurements were taken as the Luneburg lens and WG were rotated at 1^o increments in the ϕ direction. To simulate different feed locations, measurements were taken with the WG position varied along the backside of the lens (Figure 21a).

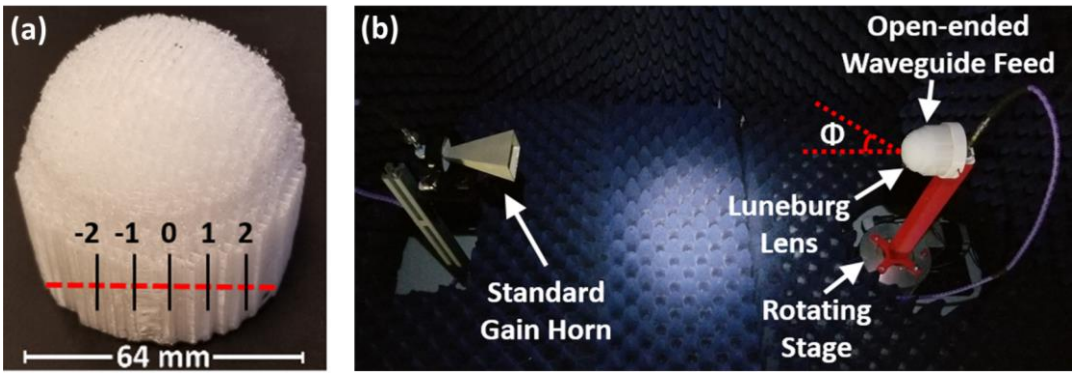

Figure 5.21: (a) Fabricated Luneburg lens with markings indicating the five positions used to place the waveguide feed. (b) System used to measure the lens' radiation pattern.

Gain pattern measurements are shown in Figure 5.22. In Figure 5.22(a), the Luneburg lens gain is plotted from 18-40 GHz. As expected the measured gain increases as the frequency increases. In Figure 5.22(b), the measured lens gain is presented as a function of frequency and elevation angle ϕ. For this measurement, the WG feed was placed at the center position (i.e., position 0 in Figure 5.21(a)). It is worth noting that the direction of the radiated beam does not vary with frequency. This is true over a considerably wide frequency band. In Figure 5.22(c), the measured lens antenna gain pattern is presented as the WG feed is shifted from the center towards the edge of the lens. As expected, the beam steers as the feed location moves away from the center line. With my fabricated lens, I achieved nearly 60 degrees of beamsteering over a wide bandwidth.

5.3.2.2 Antenna Feed Array and Power Detection

It is advantageous to design an antenna feed that leverages, as much as possible, the large bandwidth offered by the broadband nature of the Luneburg lens.

However, the feed antennas must also be physically small so as many as possible can be incorporated along the backside of the lens. Thus, for my design, I chose a bowtie antenna that presented a good compromise between bandwidth and size [50]. The antenna feed, shown in Figure 5.23(a), is less than 4 mm in size and is reasonably well matched (i.e., $|S_{11}| < -10$dB) from 20 GHz to 40 GHz.

I designed and fabricated a feed array consisting of 14 bowtie antennas, shown in Figure 5.24(a), placed along the flat side of the Luneburg lens. Using this arrangement, RF energy incident from a range of elevation and azimuth directions is focused onto the backside of the Luneburg lens and simultaneously detected. The RF output from each bowtie antenna is fed directly into a LTC5596 RMS power detector chip, which converts RF input power into a DC output voltage proportional to the RF intensity. The measured output voltages are then digitally sampled and wirelessly transmitted, via Bluetooth, to a smartphone running a custom application that records and displays the received power intensity at each feed antenna (Figure 5.26(b, c)). The entire system is powered by a 3.7V lithium polymer battery. Figure 5.24 presents the final system consisting of the Luneburg lens, antenna feed array, and electronics.

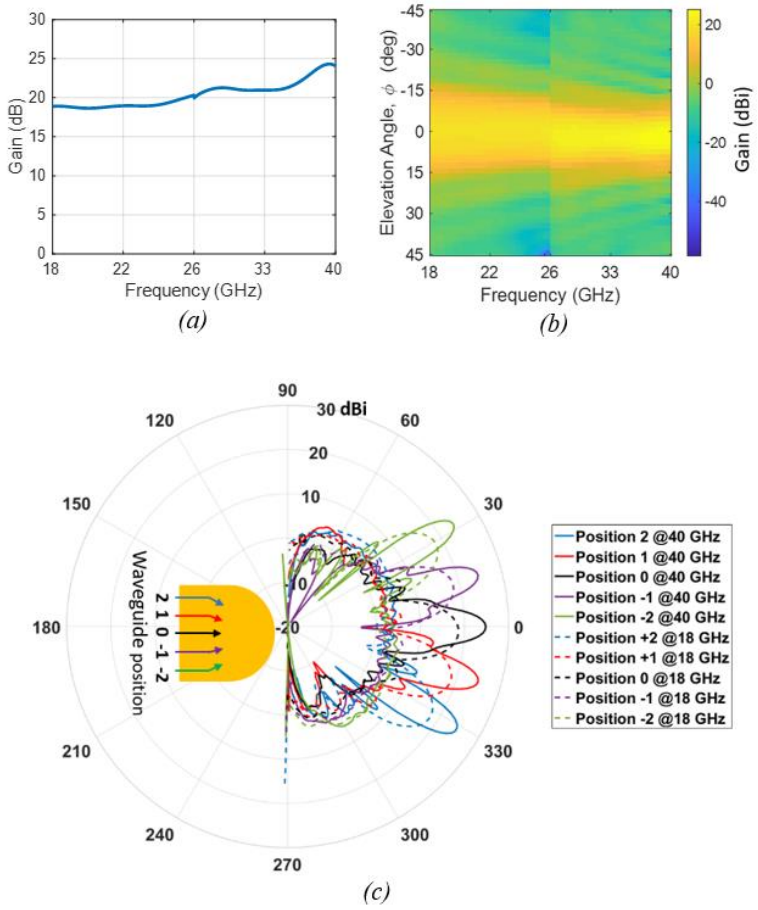

Figure 5.22: (a, b) Measured gain of Luneburg lens across Ku and Ka bands with WG at position 0. (c) Measured gain at various positions of WG feed.

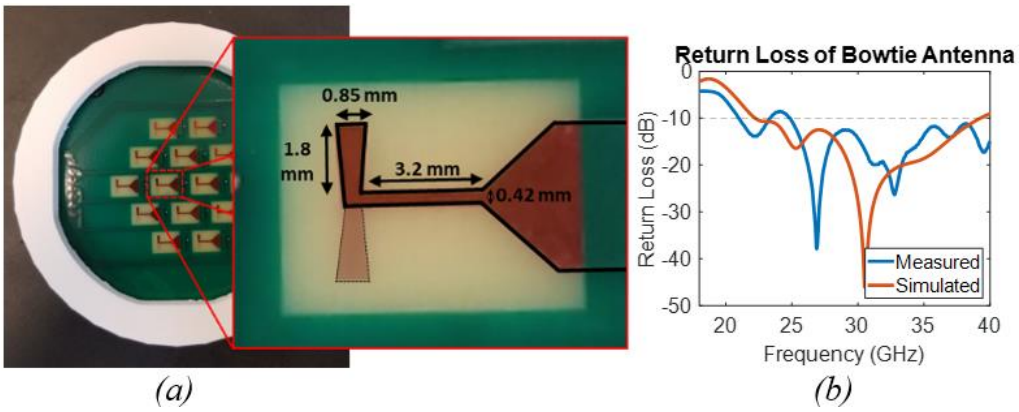

Figure 5.23: (a) Bowtie feed array design. (b) Measured and simulated return loss of bowtie feed antenna

Figure 5.24: Overview of power detecting system. (a) Close up of antenna matrix. (b) Microcontroller/BT, battery, PCB antennas, and Luneburg lens enclosure.

Experimental evaluation of system performance was done to ensure the system was operating as anticipated. I first calibrated my system using a calibrated 5 mW, 24.15 GHz source placed at various distances from the Luneburg lens. Figure 5.25(a) compares the predicted and measured incident power detected by my system as a function of source distance. Using this data, I determined the minimum detectable

power density within various well known frequency bands (Figure 5.25(b)). It should be noted that these values assume no RF amplification and would improve, at an additional cost, by including a low noise amplifier as part of the system design.

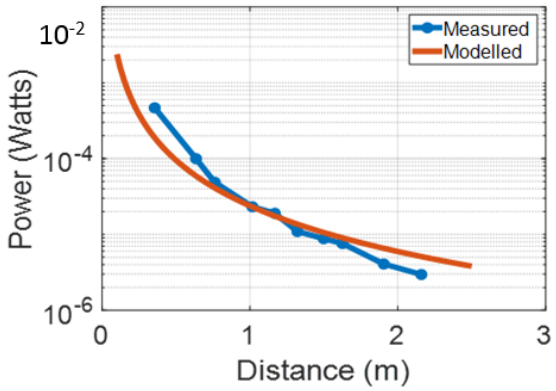

Figure 5.25: Experimental characterization results. Predicted versus measured received power using a calibrated source at various source distances

Table 5.1: Calculated minimum detectable power densities the system can detect

Minimum Detectable Power Density for 64mm Luneburg Lens	
No Amplifier	30 dB Amplifier
210.1 $\mu W/m^2$	210.1 nW/m^2

I, then, measured how the fabricated Luneburg lens focuses and detects incident power originating from various directions (Figure 5.26a). For this example, a 24.15 GHz source connected to a standard gain horn was moved to two different locations while the system response was recorded and displayed.

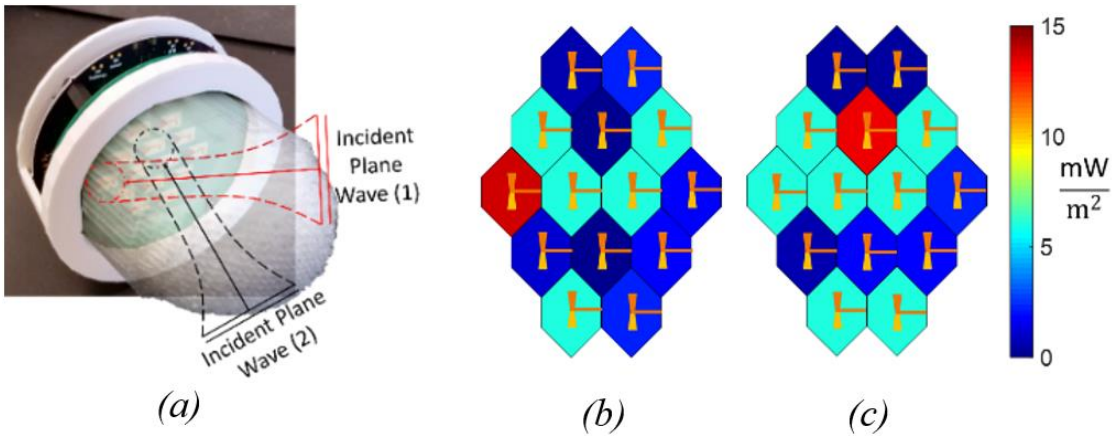

Figure 5.26: (a) Model of lens/antenna array with two incident RF sources. (b, c) Measured power density produced by incident plane waves at 24.15 GHz: (b) wave #1 at 0° elevation and 35° azimuth, and (c) wave #2 at 22° elevation and 0° azimuth.

5.3.3 Conclusion

In this application, I described a Luneburg lens based system for detecting multiple RF emitters over a reasonably large frequency band. My design leverages advancements in additive manufacturing to realize the graded index distribution of the Luneburg lens. Combining this lens with an array of small receive antennas and associated electronics creates a system that can detect multiple RF emitters with a low material cost and a simple electronic design. These advantages make my system a low-cost alternative to active beamforming for detection and tracking applications.

Chapter 6

CONCLUSION AND FUTURE WORK

6.1 Future Work

In this dissertation, I described several related research efforts aimed at designing and fabricating passive graded index structures that leverage additive manufacturing methods. Specifically, I described; (1) a structural 2D Luneburg lens based beamformer that was fabricated using a custom designed and built dry powder printer, (2) a graded index based wideband retroreflector and (3) a 3D Luneburg lens based beamformer for RF directional finding and tracking. Through this research, I was able to demonstrate both computationally and experimentally that good performance can be achieved over a broad band of frequencies by leveraging additive manufacturing methods to design and construct practical GRIN structures in 2D and 3D.

While there are several areas in which this work can be expanded upon the application that has, I believe, the most promise is the Luneburg lens based direction finder. Some current limitations to the direction finder include; (1) it is currently limited to linear polarization, (2) the current field of view is only ±35 degrees in elevation/azimuth and (3) the gain performance decreases for antenna positions further away from the center of the lens. To overcome these limitations there are several approaches. First, a modified feed antenna can be designed to be sensitive to both polarization states. This could be achieved by simply stacking bowtie antennas aligned orthogonally to each other. To support a larger FOV, two methods can be envisioned;

(1) a modified lens design with a larger scan angle and (2) using cascaded Luneburg lenses to expand the field of view. In order to overcome the weaker gain performance on the edge of the Luneburg lens, a modified Luneburg lens with a planar focal/excitation face could be designed. Similar work is described in [51]. By combining all these proposed revisions to the RF Direction Finder, the work described in this dissertation would be more useful in a wider range of real world applications.

6.2 Conclusion

The work discussed in this dissertation demonstrates that additive manufacturing is a viable solution for fabricating RF functional systems. The powder printer is a method for creating mechanically robust graded refractive index systems. The printing resolution is not as impressive as commercially available state of the art additive manufacturing systems, but it has significantly greater mechanical strength in comparison.

The Ultra-Wideband RF Retroreflector and the Ultra-Wideband RF Directional Finder leveraged a state of the art additive manufacturing system (nScrypt 3Dn-300). In both of these systems, an additively manufactured Luneburg lens was used for high gain passive beamforming. The performance of these systems was comparable to the effectiveness of a parabolic dish antenna of a similar size. This impressive performance demonstrates that additively manufactured RF systems could be used as an alternative to traditional systems.

REFERENCES

1. Cichon, Dieter J., and Wiener Wiesbeck. "The Heinrich Hertz wireless experiments at Karlsruhe in the view of modern communication." (1995): 1-6.

2. L. Brown, *A Radar History of World War II: Technical and Military Imperatives*. Philadelphia, PA, USA: Institute of Physics, 1999.

3. Wolff, Christian. “Strategic Radar Systems.” *Radar Basics - AN/FPS-108* "Cobra Dane", www.radartutorial.eu/19.kartei/01.oth/karte003.en.html.

4. Wolff, Christian. “Strategic Radar Systems.” *Radar Basics - AN/FPS-115* "Pave Paws", www.radartutorial.eu/19.kartei/01.oth/karte004.en.html.

5. “AN/SPY-1D.” *AN/SPY-1D*, www.deagel.com/Sensor-Systems/ANSPY-1D_a001523003.aspx.

6. “Raytheon completes upgrades to BMEWS radar in Alaska 16-Mar-01”, http://radomes.org/museum/documents/BMEWSSite2ClearAKnewradar032001.html

7. “GAO U.S. Government Accountability Office” *MISSILE DEFENSE: Air Force Report to Congress Included Information on the Capabilities, Operational Availability, and Funding Plan for Cobra Dane,* https://www.gao.gov/products/GAO-19-68

8. Luneburg, Rudolf K. “Mathematical Theory of Optics”. University of California Press, 1966

9. Gaufillet, Fabian, and Eric Akmansoy. "Maxwell Fish-Eye and Half-Maxwell Fish-Eye Based on Graded Photonic Crystals." *IEEE Photonics Journal* 10.3 (2018): 1-10.

10. Zhang, Shiyu. "3D printed dielectric Fresnel lens." *2016 10th European Conference on Antennas and Propagation (EuCAP)*. IEEE, 2016.

11. Vieira Hoel, Karina & Kristoffersen, Stein & Jastram, Nathan & Filipovic, Dejan. (2017). *3D printed Rotman lens*. 125-128. 10.23919/EuMC.2017.8230815.

12. “Luneburg Antenna.” *Luneburg Antenna - Engineering and Technology History Wiki*, ethw.org/Luneburg_Antenna.

13. Greenwood, Andrew D., and Jian-Ming Jin. "A field picture of wave propagation in inhomogeneous dielectric lenses." *IEEE Antennas and Propagation Magazine* 41.5 (1999): 9-18

14. Kim, Yong Hyeon, Willy Anugrah Cahyadi, and Yeon Ho Chung. "Experimental demonstration of VLC-based vehicle-to-vehicle communications under fog conditions." *IEEE Photonics Journal* 7.6 (2015): 1-9.

15. Gleaves, Mike. “Rotman Lens' Electronic Beam Steering Aims At 5G Signals.” *Microwaves & Radio Frequency*, 7 Feb. 2018, www.mwrf.com/components/rotman-lens-electronic-beam-steering-aims-5g-signals.

16. Johari, Esha, Zubair Akhter, and M. Jaleel Akhtar. "Design of the modified cylindrical Luneberg lens antenna for millimeter wave imaging." *2015 IEEE International Symposium on Antennas and Propagation & USNC/URSI National Radio Science Meeting*. IEEE, 2015.

17. Rondineau, Sébastien, Mohamed Himdi, and Jacques Sorieux. "A sliced spherical Luneburg lens." *IEEE Antennas and Wireless Propagation Letters* 2 (2003): 163-166.

18. Bor, Jonathan, et al. "Foam based Luneburg lens antenna at 60 GHz." *Progress In Electromagnetics Research Letters* 44 (2014): 1-7.

19. Matytsine, Leo, et al. "Large size, lightweight, Luneburg Lenses for multi-beam antenna applications." *2012 6th European Conference on Antennas and Propagation (EUCAP)*. IEEE, 2012.

20. Reinholdt, Johan. "Cylindrical Luneburg lens antenna for multi-beam small cell wireless backhaul applications." Thesis. (2014).

21. M. Imbert, A. Papió, F. De Flaviis, L. Jofre, and J. Romeu. *Design and Performance Evaluation of a Dielectric Flat Lens Antenna for Millimeter-Wave Applications*. IEEE Antennas and Wireless Propagation Letters: Vol. 14, pp. 342-345.

22. M. Mirotznik, B. Good, P. Ransom, D. Wikner, and J. Mait. *Broadband Antireflective Properties of Inverse Motheye Surfaces. IEEE Transactions On Antennas and Propagation*: Vol. 58, no. 9, pp. 2969-2980.

23. D. Roper, B. Good, R. McCauley, S. Yarlagadda, J. Smith, A. Good, P. Pa, and M. Mirotznik. *Additive manufacturing of graded Dielectrics*. Smart Materials and Structures: Volume 23, Issue 4, March 2014.

24. "ECCOSTOCK® HiK." ECCOSTOCK® HiK500F - Emerson & Cuming Microwave Products, www.eccosorb.com/products-eccostock-hik.htm. Accessed 26 Apr. 2017."TenCate." TenCate BTCy-1 PIP | Royal Ten Cate Divisions EMEA. Web. 26 Apr. 2017.

25. "RF/Microwave Absorbers." Eccostock HiK Powder | LairdTech, www.lairdtech.com/products/eccostock-hik-powder. Accessed 26 Apr. 2017.

26. S. Yang, and J. Evans. *Acoustic control of powder dispensing in open tubes*. Powder Technology: Vol 139, pp. 55-60.

27. S. Yang and J. Evans. *Metering and dispensing of powder: the quest for new solid free forming techniques*. Powder Tech: 178 56–72.

28. X. Lu, S. Yang, and J. Evans. *Microfeeding with different ultrasonic nozzle designs. Ultrasonics*: Vol 49, pp. 514-521.

29. S. Yang, and J. Evans. *Metering and dispensing of powder*. Powder Technology: Vol 178, issue 1, pp. 56-72.

30. X. Lu, S. Yang, and J. Evans. *Dose uniformity of fine powders in ultrasonic microfeeding*. Powder Technology: Vol. 175, pp. 63-72.

31. X. Lu, S. Yang, and J. Evans. *Ultrasound-assisted microfeeding of fine powders*. Particuology: Vol. 6, pp. 2-8.

32. S. Yang and J. Evans. *A dry powder jet printer for dispensing and combinatorial research*. Powder Technology: Vol. 142, pp. 219-222.

33. W. Merrill, R. Diaz, M. LoRe, M. Squires, and N. Alexopoulos. *Effective Medium Theories for Artificial Materials Composed of Multiple Sizes of Spherical Inclusions in a Host Continuum*. IEEE Transactions on Antennas and Propagation. Vol. 47, No. 1, January 1999.

34. A. Sihvola. *Homogenization of a Dielectric Mixtre with Anisotropic Spheres in Anisotropic Background*. Vol. TEAT-7050. January 1996.

35. D. Pozar. Microwave Engineering. Hoboken, NJ 2005. John Wiley & Sons, Inc, 2012, pp 144.

36. S. Orfanidis. *Electromagnetic Waves and Antennas*. 2014, pp. 227-231, pp. 193-203 [Online]. Available: www.ece.rutgers.edu/~orfanidi/ewa

37. M. Liang, W. Ng, K. Chang, K. Gbele, M. Gehm, and H. Xin. *A 3-D Luneburg Lens Antenna Fabricated by Polymer Jetting Rapid Prototyping*. IEEE Transactions on Antennas and Propagation, Vol. 62, No. 4, April 2014.

38. S. Baev, S. Gechev, B. Hadjistamov, and P. Dankov. *Modeling and Simulations of Luneburg Lens Antennas for Communcation Purposes*. 16th Telecommunications forum TELFOR, 2008.

39. Kurimoto, Muneaki, et al. "Dielectric properties and 3d printing of uv-cured acrylic composite with alumina microfiller." *IEEE Transactions on Dielectrics and Electrical Insulation* 23.5 (2016): 2985-2992.

40. Hilbert, David. "Über die stetige Abbildung einer Linie auf ein Flächenstück." Dritter Band: Analysis· Grundlagen der Mathematik· Physik Verschiedenes. Springer, Berlin, Heidelberg, 1935. 1-2.

41. Peano, Giuseppe. "Sur une courbe, qui remplit toute une aire plane." Mathematische Annalen36.1 (1890): 157-160.

42. Larimore, Zachary, et al. "Use of space-filling curves for additive manufacturing of three dimensionally varying graded dielectric structures using fused deposition modeling." *Additive Manufacturing* 15 (2017): 48-56.

43. Regazzoni, Carlo S., and Andrea Teschioni. "A new approach to vector median filtering based on space filling curves." *IEEE Transactions on Image Processing* 6.7 (1997): 1025-1037.

44. Schultz, John W. *Focused Beam Methods: Measuring Microwave Materials in Free Space*. CreateSpace Independent Publishing Platform, 2012.

45. S. D. Robertson, "Targets for microwave radar navigation," in *The Bell System Technical Journal*, vol. 26, no. 4, pp. 852-869, Oct. 1947.

46. J. L.'Bohnert and H. P. Coleman. "Applications of the Luneburg lens." Naval Research Lab, Washington, D.C., Report 4888, March 7, 1957.

47. G. Peeler and H. Coleman, "Microwave stepped-index Luneburg lenses," in *IRE Transactions on Antennas and Propagation*, vol. 6, no. 2, pp. 202-207, April 1958.

48. Z. Larimore, S. Jensen, A. Good, A. Lu, J. Suarez and M. Mirotznik, "Additive Manufacturing of Luneburg Lens Antennas Using Space-Filling Curves and Fused Filament Fabrication," in *IEEE Transactions on Antennas and Propagation*, vol. 66, no. 6, pp. 2818-2827, June 2018.

49. E. F. Knott, J. Shaeffer, and M. Tuley, "Radar Cross Section, 2nd edition", SciTech Publishing, pp. 480-484, 2004.

50. M. Z. A. Abdul Aziz M. K. A. Rahim. "Bow-Tie Microstrip Antenna Design." 2005 13th IEEE International Conference on Networks Jointly Held with the 2005 IEEE 7th Malaysia International Conference on Communications, doi:10.1109/icon.2005.1635425.

51. Biswas, Soumitra, et al. "Realization of modified Luneburg lens antenna using quasi-conformal transformation optics and additive manufacturing." *Microwave and Optical Technology Letters* 61.4 (2019): 1022-1029.

Appendix A

Permission for Reuse

Order Notes

Austin Good: **Date:** Apr 24, 2019 11:03:05 AM

The title of the IOP article is: Multifunctional graded dielectrics fabricated using dry powder printing

DOI link: https://doi.org/10.1088/1361-665X/aa782b

Rights and Permissions: **Date:** Apr 24, 2019 9:31:40 AM

Thank you for your request. In order that we can process your request, I should be grateful if you could provide the title of the IOP article you wish to reuse and a link via DOI where possible. I could not identify this from the information above

---

CLOSE WINDOW

IOP Publishing LICENSE
TERMS AND CONDITIONS

Jun 19, 2019

This is a License Agreement between University of Delaware -- Austin Good ("You") and IOP Publishing ("IOP Publishing") provided by Copyright Clearance Center ("CCC"). The license consists of your order details, the terms and conditions provided by IOP Publishing, and the payment terms and conditions.

All payments must be made in full to CCC. For payment instructions, please see information listed at the bottom of this form.

License Number	4611981165451
License date	Apr 15, 2019
Licensed content publisher	IOP Publishing
Licensed content title	Smart Materials and Structures
Licensed content date	Jan 1, 1992
Type of Use	Thesis/Dissertation
Requestor type	Author of requested content
Format	Print
Portion	chapter/article
The requesting person/organization is:	Austin Good/University of Delaware
Title or numeric reference of the portion(s)	Entire publication
Title of the article or chapter the portion is from	N/A
Editor of portion(s)	N/A
Author of portion(s)	N/A
Volume of serial or monograph.	N/A
Page range of the portion	
Publication date of portion	end 2019
Rights for	Main product
Duration of use	Life of current edition
Creation of copies for the disabled	no
With minor editing privileges	yes
For distribution to	Worldwide
In the following language(s)	Original language of publication
With incidental promotional use	no
The lifetime unit quantity of new product	Up to 499
Title	ADDITIVE MANUFACTURING OF PASSIVE BEAMFORMING SYSTEMS

Institution name	University of Delaware
Expected presentation date	May 2019
Billing Type	Invoice
Billing Address	University of Delaware 139 THE GREEN EVANS HALL RM 140 Newark, DE 19716 United States Attn: Austin Good
Total (may include CCC user fee)	0.00 USD